Citation for published version:
Burke, R, Giedymin, A, Wu, Z, Chuan, H, Bourne, N & Hawley, G 2020, 'A Lumped Parameter Thermal Model for Single Sided AFPM Machines with Experimental Validation', *IEEE Transactions on Transportation Electrification*, vol. 6, no. 3, pp. 1065-1083. https://doi.org/10.1109/TTE.2020.2998110

DOI:
10.1109/TTE.2020.2998110

Publication date:
2020

Document Version
Peer reviewed version

Link to publication

© 2020 IEEE. Personal use of this material is permitted. Permission from IEEE must be obtained for all other users, including reprinting/ republishing this material for advertising or promotional purposes, creating new collective works for resale or redistribution to servers or lists, or reuse of any copyrighted components of this work in other works.

University of Bath

Alternative formats
If you require this document in an alternative format, please contact:
openaccess@bath.ac.uk

General rights
Copyright and moral rights for the publications made accessible in the public portal are retained by the authors and/or other copyright owners and it is a condition of accessing publications that users recognise and abide by the legal requirements associated with these rights.

Take down policy
If you believe that this document breaches copyright please contact us providing details, and we will remove access to the work immediately and investigate your claim.

Download date: 05. May. 2023

A Lumped Parameter Thermal Model for Single Sided AFPM Machines with Experimental Validation

Richard Burke[1], Artur Giedymin[2], Zhongze Wu[1*], Hawwooi Chuan[1], Nick Bourne[1] and Gary Hawley[1]

1. Institute for Advanced Automotive Propulsion Systems, University of Bath, BA2 7AY, Bath, UK
2. Institut für Energie und Automatisierungstechnik, Fachgebiet Elektrische Antriebstechnik, Technische Universität Berlin, 10587 Berlin, Germany

*Corresponding Author contact. Email: z.wu@bath.ac.uk, Tel: +441225383062

ABSTRACT

Axial flux permanent magnet (AFPM) machines are promising for hybrid electric vehicles (HEVs) due to the compactness, high torque density and high efficiency. However, poor thermal characterization leads to an over-sizing of these machines which ultimately compromises overall system efficiency. In this paper, the transient thermal behaviour of all the components in the single sided AFPM machine are characterized in an accurate but computationally efficient lumped parameter thermal model (LPTM). For the first time, contact measurements on the rotor have been used in AFPM machines to demonstrate the ability of the model to predict all component temperatures to within 4 °C for steady state. The mean temperature error over a load step transient was less than 5°C with a maximum error less than 13.5 °C which was for the winding. The model has a running time of approximately 1000 times faster than real time on a desktop machine and is suitable for integration into system simulation tools and predictive control strategies to avoid over-sizing of the motor and improve the usage of the electric machine in dynamic duty cycles.

Keywords: Axial flux permanent magnet machine; DC current test; finite element analysis; lumped parameter thermal model; thermal capacity; thermal resistance.

1 INTRODUCTION

Propulsion system electrification is critical to delivering clean and sustainable transportation and rare-earth permanent magnet (PM) machines are ideally suited to this application owing to their high energy density [1]-[5]. However, poor thermal characterization of these machines can lead to higher design safety factors which in turn results in larger motors being used for a given power requirement where smaller motors would have been sufficient [6], [7]. For a vehicle, the larger motor will increase overall weight and will likely increase costs. It will also have consequences for the rest of the propulsion system which will ultimately lead to compromises on cost, packaging, and performance. For example, in an electric vehicle (EV), using a larger motor and larger power electronics will increase vehicle weight and limit the space for the energy storage, both contributing to an overall lower vehicle range.

Electric motors are typically specified with both peak and continuous power ratings. The continuous power rating can be maintained without overheating issues whereas the peak power can only be delivered intermittently. Conventional propulsion system modelling tools [8]-[12] simulate the electric machine as a quasi-steady model, usually in the form of a look-up table characterizing motor efficiency. As there is no indication of the thermal behaviour, this could lead to a motor being selected based on its continuous rather than its peak power rating. This approach will directly lead to the over-engineering scenario described above. The extent of the over-sizing will much depend on the type of cooling that is used within the specific motor technology for that application. In the case of air-cooled machine, the peak power can be more than double that of the continuous power. For given specific magnetic and electrical loadings, motor torque is proportional to motor volume [13]. Hence, for a given motor technology, speed rating and cooling design, motor volume and mass are approximately proportional to rated power. It can therefore be expected that the subsequent motor would be oversized by a factor of 2 [14].

If a smaller motor has been selected, then in service it is vital that the powertrain controller has knowledge of this limitation in order to optimise its use. A computationally efficient model of the thermal behaviour will therefore enable the creation of new system control strategies to manage motor power demand, including online optimal controllers such as model predictive control (MPC) [15]. These are particularly interesting for hybrid propulsion systems where the controller is continuously making decisions on the power split between the combustion engine and the electric machine.

This paper aims to construct and experimentally validate under steady and transient conditions a computationally efficient model of the thermal behaviour of all the components in the single sided axial flux permanent magnet (AFPM) machine. This paper is organized as follows: In section II, a review of previous work and models will be presented. In section III, the machine topology, modelling, and experimental approaches are presented. In section IV, the parameterization of the lumped parameter thermal model (LPTM) is explained, exemplified for the 1.5 kW three-phase 24-slot/8-pole single side AFPM machine and in section V the model is compared with experiments. Finally, the conclusions are captured in section VI.

2 BACKGROUND

Although different topologies of AFPM machine exist [16]-[20], the compactness of the machine means that heat losses are concentrated in a smaller area. At the same time, both the rotor and stator have temperature limitations due to degradation of the winding coils, demagnetization of the PMs and mechanical weaknesses in the bonded joints [21].

Multi-dimensional models are regularly used to predict temperatures in electric machines; however they have long execution times and are typically useful and accurate for predicting steady state conditions at the limit of the operating range of the machine [22]-[24]. These are not suited for modelling of full propulsion systems over transient duty cycles such as those seen in vehicles and

there is a need for a more effective modelling approach [25]. Simplified mathematical models of electric machines are less common because the process to construct such a model is not trivial. Lumped capacitance or thermal network modelling will be used in this work where the system is represented as a series of thermal nodes (incorporating thermal capacitances), linked via thermal resistances. The complexity of these models is linked to the number of thermal nodes with more thermal nodes increasing the model run time and increasing the task of model parameterisation. Table 1 presents a summary of works published relating to this type of model for different motor types.

Table 1: Comparison of LPTMs for PM Machines

Machine type	References	Steady-state or transient-state?	Node number	Rotor temperature measurement?	Max. absolute error at steady-state (°C)	Max. absolute error at transient-state (°C)
Single-sided AFPM	[22], [28]	Steady-state	7	Infrared camera	~3 (Winding)	N/A
	[21]	Steady-state	13	Infrared camera	4 (Winding)	N/A
	[26]	Transient-state	250	No	Not Given	
	[29]	Transient-state	5	No	No experimental validation	
	[30]	Stator only	unknown	Not fitted	Not given	2.4 (unknown)
YASA AFPM	[31]	Transient-state	26	No	No experimental validation	
Kaman AFPM	[32]	Transient-state	19	No	Not given	~10 (stator yoke)
	[33]	Transient-state	25 - 35	No	Not Given	4.7 (end winding)
SPM without rotor sleeve	[34]	Transient-state	12	No	Not Given	25 (Winding)
	[35]	Transient-state	>35	No	Not Given	~10 (Shaft)
SPM with rotor sleeve	[36]	Transient-state	6	Slip ring unit	Not Given	~20 (Sleeve)
IPM	[37]	Transient-state	~30	Not Given	5 (Magnet)	Not Given
PMaSynRM	[38]	Transient-state	~55	Slip ring unit	~10 (Winding)	Not Given

A 3-D LPTM is proposed [26] to analyse the steady-state thermal performance of the single sided AFPM machine, based on the general cuboidal element [27]. However, this 3-D LPTM is complicated with 250 nodes, which is not suitable for the optimization of the model-based control strategies for the electric powertrain. 2-D steady-state LPTMs without consideration of thermal capacities for the single sided AFPM machine is analysed in [21], [22] and [28], with the node number of 13 and 7, respectively. In [29], a simple 2-D transient-state LPTM is proposed for the single sided AFPM machine, however, the shaft and different materials inside the stator slot, including copper,

isolation, resin and liner, are not included in the LPTM. In addition, there is no experimental validation of the transient-state LPTM in [29]. In [30], the Monte Carlo method is applied to optimize the heat transfer parameters at the boundaries of the transient state LPTM for the single sided AFPM machine. By using the Monte Carlo method, the LPTM can achieve a maximum absolute error of stator temperature of 2.4 °C during constant DC current test. However, this model only analyses the stator.

The LPTMs have also been applied in other types of AFPM machines to predict the temperatures. In [31], a transient state LPTM is proposed for the yokeless and segmented armature (YASA) type AFPM machine, with 20 nodes for the stator and 6 nodes for the rotor. The temperature profiles of the short-time duty and the intermittent duty of a 4 kW YASA AFPM machine are presented, however there is no experimental validation. In [32], a transient state LPTM with 19 nodes is proposed for the Kaman type AFPM machine, i.e. stator-rotor-stator topology. This model achieves a maximum temperature error in transient state of around 10 °C at the stator yoke. In [33], a cuboidal element based 3-D transient LPTM is proposed, also for the Kaman type AFPM machine. The maximum absolute error between the LPTM and the experiments at steady state occurs at the end winding top coil, i.e. 4.7 °C. None of these papers present experimental validation of rotor and magnet temperatures.

The results presented in Table 1 clearly identify a lack of transiently validated thermal model of the single side AFPM, with small number of thermal nodes. The results here will be used as a benchmark for the model presented within this work.

3 METHODOLOGY

The main focus of this study is the construction and validation of a LPTM for an AFPM machine. Firstly, the model will be validated over a simple transient operating condition with experiments

measuring both stator and rotor temperatures. Secondly, the modelling approach will be applied to a similar motor and validated over a highly dynamic duty cycle.

The thermal model will be constructed for a three-phase 24-slot/8-pole integral slot single sided AFPM machine. The aim is to create and parameterize a LPTM with high level of accuracy in terms of temperature prediction whilst providing a run time and calculation overhead that is suitable for powertrain systems optimization and control. To first develop a fundamental understanding of the heat flows in the motor, the machine is analysed both experimentally and using finite element (FE) simulation. 2-D and 3-D simulation were conducted with ANSYS Maxwell suite to provide key inputs to the LPTM. Experiments were conducted on an instrumented motor which includes measurements on the motor stator and rotor using a bespoke wireless sensing system. The experiments are conducted firstly to measure external heat losses and secondly to provide validation data to assess the accuracy of the LPTM.

3.1 Machine Topology

The machine analysed in this work is an AFPM machine shown in Figure 1. It is important to note the coordinate system used in this figure, as it will be referred to systematically as the LPTM is presented. The machine is a three-phase integral slot 24-slot/8-pole machine, of which the specifications are shown in Table 2.

Table 2: AFPM Test Motor Specifications from Manufacturer

Item	Value	Unit
Motor type	PMS 100 RF	-
PM type	N35UH	-
Phase winding resistance at 20°C, R_{ph}	22.65	mΩ
Slot number, Q	24	-
Pole-pair number, p	4	-
Rated power, P_n	1500	W
Rated torque, T_n	3.18	Nm
Rated speed, Ω_n	4500	rpm
Rated line RMS current, I_{ln}	37.2	A
Rated efficiency, η_n	89.9	%
Machine housing diameter, D_c	200	mm
Machine housing length, l_c	55	mm

3.2 Lumped Parameter Thermal Model Description

3.2.1 Model Overview

Due to an axis of symmetry, the thermal model can be constructed to simulate a segment of the AFPM machine, as shown in Figure 2. The motor is broken down into three key components:

1. The rotor (including magnets, shaft, and main bearings)
2. The stator (including the windings)
3. The housing

The model comprises of seven heat sources which correspond to the losses of the motor. These are connected to the relevant parts of the machine as follows:

1. Rotor: two bearing friction losses P_{b1} and P_{b2}, magnet eddy current losses P_m, rotor iron loss P_{ri} and windage losses P_{wd}
2. Stator: Copper loss P_{cu} and stator iron loss P_{si}

The rotor and stator are linked via the convective heat transfer in the airgap. The stator is linked to the housing via conduction, and the rotor also exchanges heat with the housing via conduction through the bearings. The housing itself exchanges heat with its surrounding via conduction at the mounting plate and convection to the surrounding air.

3.2.2 Stator Thermal Model

The stator shown in Figure 3 is initially simplified into a 2-D geometry as shown in Figure 4a. The goal is that the upper object and the lower object in Figure 4a have the same volume. Based on this approach, the analysed AFPM machine shown in Figure 1 can be transformed to a linear model for 2-D analysis, as show in Figure 4b.

Each slot is filled with a liner material around the edge of the slot and a matrix of copper wires sitting within a resin, as shown in Figure 5a. Due to the random nature of the position of each

copper conductor, it is not necessary to describe each conductor separately. This assumption yields a layered winding model as described in [39] where the individual winding is assumed to have a homogeneous thermal resistance (Figure 5b). These stator dimensional parameters shown in Figure 5 are listed in Table 3, which can be referred in the machine cross-section shown in Figure 9.

The slot thermal model is shown in Figure 6. Each slot is connected to one heat source which is the slot winding losses ($P_{w,slot}$) calculated in equation (1) as the fraction of total winding losses occurring in each slot.

$$P_{W,slot} = \frac{P_W}{Q} \tag{1}$$

The slot is linked to the two adjacent stator teeth through resistances in the *x*-direction (R_{cirx}). The slot is also linked to the stator yoke and the air gap through resistances in the *y*-direction R_{ciry}. Both R_{cirx} and R_{ciry} are the serial connections of the thermal resistances of the copper, isolation and resin in *x*- and *y*-direction, respectively (equation (2)). The *x* and *y* coordinates refer to those presented in Figure 1, where *x* is the circumferential heat flow and *y* is the axial heat flow.

$$\begin{cases} R_{cirx} = R_{cx} + R_{ix} + R_{rx} \\ R_{ciry} = R_{cy} + R_{iy} + R_{ry} \end{cases} \tag{2}$$

The thermal resistance terms for copper in equation (2) are obtained using Fourier's law for one dimensional heat transfer applied to both the *x*- and *y*- directions,

$$R = \frac{\Delta x}{A \times k} \tag{3}$$

where *R* is the absolute thermal resistance across the thickness of the sample Δx, *A* is the cross-section area of the sample, and *k* is the thermal conductivity of the sample.

Equation (3) is applied specifically to the copper windings in the *x*- and *y*-direction in equation (4) where:

- The thermal conductivity is that of copper, k_c.
- In the *x*-direction, the 1-D distance, Δx_c, is calculated as half of the slot width (W_s), multiplied by the copper winding filling factor f_c. The heat transfer area, A_{cx}, is the slot height (H_s) multiplied by the slot length (L_s).
- Similarly, in the *y*-direction, the 1-D distance, Δy_c, is calculated as half of the slot height (H_s), multiplied by the copper winding filling factor f_c. Again, the heat transfer area, A_{cy}, is the slot width (W_s) multiplied by the slot length (L_s).

$$\begin{cases} R_{cx} = \dfrac{\Delta x_c}{A_{cx} \times k_c} = \dfrac{\left(\dfrac{f_c W_s}{2}\right)}{(L_s H_s) \times k_c} \\ R_{cy} = \dfrac{\Delta y_c}{A_{cy} \times k_c} = \dfrac{\left(\dfrac{f_c H_s}{2}\right)}{(L_s W_s) \times k_c} \end{cases} \quad (4)$$

Similar to equation (4), the thermal resistances of resin in *x*- and *y*-direction R_{rx} and R_{ry} can be obtained by replacing f_c with the effective filling factor for resin (f_r) and isolation (f_i) and k_c with the thermal conductivity of resin (k_r) and isolation (k_i).

The thermal resistances of liner in *x*- and *y*-direction in Figure 6 are given by equation (5), where k_l is the thermal conductivity of liner.

$$\begin{cases} R_{lx} = \dfrac{W_l}{L_s H_s k_l} = \dfrac{W_l}{L_s H_s k_l} \\ R_{ly} = \dfrac{W_l}{L_s W_s k_l} = \dfrac{W_l}{L_s W_s k_l} \end{cases} \quad (5)$$

The thermal capacity of a motor element C_X is given by equation (6) where c_X and m_X thermal specific capacity and mass of that motor element.

$$C_X = c_X m_X \quad (6)$$

The complete stator thermal model is shown in Figure 7, including both stator back (or stator yoke) and stator tooth. It should be noted that in this representation all of the slots and teeth have been consolidated into a single thermal node for each. To do this, the two resistance paths from the slot to adjacent teeth have been consolidated into a one connexion, equivalent to two resistances connected in parallel. Equally, all of the slots have been consolidated into a single resistance composed of 24 parallel resistances. This allows the winding losses (P_w) to replace the slot winding losses ($P_{w,slot}$).

The full stator representation introduces the stator iron losses P_{si}. In Figure 7, R_{sby} is the thermal resistance of the stator back in *y*-direction, which is given by equation (7), where H_{sb}, W_{sb} and L_{sb} are the height, width and length of the stator back, respectively. k_{si} is the thermal conductivity of the stator iron.

$$R_{sby} = \frac{H_{sb}/2}{W_{sb}L_{sb}k_{si}} = \frac{H_{sb}}{2W_{sb}L_{sb}k_{si}} \qquad (7)$$

Similarly in Figure 7, R_{stx} and R_{sty} are the thermal resistance of the stator teeth in *x*- and *y*-direction, which are given by equation (8), where H_{st}, W_{st} and L_{st} are the height, width and length of the stator tooth, respectively.

$$\begin{cases} R_{stx} = \dfrac{W_{st}/2}{H_{st}L_{st}k_{iron}} \times \dfrac{1}{2Q} = \dfrac{W_{st}}{4QH_{st}L_{st}k_{si}} \\ R_{sty} = \dfrac{H_{st}/4}{W_{st}L_{st}k_{iron}} \times \dfrac{1}{Q} = \dfrac{H_{st}}{4QW_{st}L_{st}k_{si}} \end{cases} \qquad (8)$$

C_{sb} and C_{st} in Figure 7 are the thermal capacity of stator back and stator tooth, respectively, which can be obtained based on the equation (6) with the thermal specific capacity of the stator iron c_{si}.

3.2.3 Rotor, Shaft and Bearings Thermal Model

The magnet thermal model is shown in Figure 8, in which R_{my} is the thermal resistance in *y*-direction and C_m is the thermal capacity of PMs. P_m represents the magnet losses. C_m can be obtained based

on the equation (6) with the thermal specific capacity of permanent magnet material c_m. R_{my} is calculated using equation (9), where H_m and A_m are the height and surface area of each PM, respectively. k_m is the thermal conductivity of magnet.

$$R_{my} = \frac{H_m/2}{A_m k_m} \times \frac{1}{2p} = \frac{H_m}{4pA_m k_m} \tag{9}$$

Based on the geometry of the rotor iron shown in Figure 9, the rotor iron thermal model is given in Figure 10, in which R_{rz1}, R_{rz2}, R_{rz3} and R_{rz4} are the thermal resistances in *z*-direction of the four rotor iron parts from inside to outside. P_{ri} represents the rotor iron losses. C_r is the thermal capacity of the rotor iron. The thermal resistance R_{ry3} in *y*-direction can be calculated by equation (10), where h_{r34}, r_{r4} and r_{r3} are given in Table 3 and referred in Figure 9. k_{ri} is the thermal conductivity of the rotor iron. The rotor dimensions in Table 3 can be referred in the motor cross-section shown in Figure 9.

$$R_{ry3} = \frac{h_{r34}/2}{\pi(r_{r4} + r_{r3})(r_{r4} - r_{r3})k_{ri}} = \frac{h_{r34}}{2\pi(r_{r4}^2 - r_{r3}^2)k_{ri}} \tag{10}$$

The thermal resistance $R_{rz,i}$ (i=1,2,3,4) in *z*-direction in Figure 10 can be obtained from equation (11), where $r_{r,i}$, $r_{r,i+1}$ and $h_{r,i,i+1}$ (i=1,2,3,4) are given in Table 3 and illustrated in Figure 9.

$$R_{rz,i} = \frac{r_{r,i+1} - r_{r,i}}{2\pi\left(r_{r,i+1} + r_{r,i}\right)h_{r,i,i+1}k_{ri}} \tag{11}$$

The rotor iron thermal capacity C_r shown in Figure 10 can be given by equation (12), where C_{ri} (i=1,2,3,4) is the thermal capacity of the four rotor iron parts. m_{ri} (i=1,2,3,4) is the mass of the four rotor iron parts. ρ_r is the mass density of rotor iron.

$$\begin{aligned} C_r &= \sum_{i=1,2,3,4} C_{r,i} = c_{ri} \sum_{i=1,2,3,4} m_{r,i} \\ &= \pi c_{ri} \sum_{i=1,2,3,4} \rho_r \left(r_{r,i+1}^2 - r_{r,i}^2\right) h_{r,i,i+1} \end{aligned} \tag{12}$$

Table 3: Main Dimensional Parameters (Unit: mm unless stated)

Stator and rotor	Value	Shaft and housing	Value
Slot length, L_s	26.26	Shaft diameter 1, d_{sh1}	19
Slot height, H_s	12.80	Shaft diameter 2, d_{sh2}	20
Slot width, W_s	6.00	Shaft diameter 3, d_{sh3}	30
Liner width, W_l	0.36	Shaft diameter 4, d_{sh4}	25
Stator outer radius, r_{so}	62	Shaft diameter 5, d_{sh5}	20
Stator inner radius, r_{si}	35.3	Shaft length 1, l_{sh1}	46.2
Stator height, h_s	25	Shaft length 2, l_{sh2}	16
Stator back height, h_{sb}	8.2	Shaft length 3, l_{sh3}	20
Stator slot height, h_{ss}	8.2	Shaft length 4, l_{sh4}	19.5
Rotor radius 1, r_{r1}	12.5	Shaft length 5, l_{sh5}	15.5
Rotor radius 2, r_{r2}	20	Housing outer diameter, d_{ho123}	200
Rotor radius 3, r_{r3}	32.385	Housing inner diameter 1, d_{hi1}	52
Rotor radius 4, r_{r4}	61.5	Housing inner diameter 2, d_{hi1}	178
Rotor radius 5, r_{r5}	64.85	Housing inner diameter 3, d_{hi3}	59
Rotor height 12, h_{r12}	15	Housing length 1, l_{h1}	7.9
Rotor height 23, h_{r23}	7	Housing length 2, l_{h2}	46.55
Rotor height 34, h_{r34}	6	Housing length 3, l_{h3}	7.4
Rotor height 45, h_{r45}	7	Magnet height, H_m	3
		Magnet surface area, A_m	893.58mm^2

Based on the geometry of the shaft shown in Figure 9, the shaft thermal model is given in Figure 11, in which R_{shy1}, R_{shy2}, R_{shy3}, R_{shy4} and R_{shy5} are the thermal resistances in *y*-direction of the five shaft elements from left to right. R_{shz2}, R_{shz4} and R_{shz5} are the thermal resistances in *z*-direction of the shaft elements 2, 4 and 5. C_{sh} is the thermal capacity of the shaft, which can be obtained similar to the equation (6). The thermal resistance $R_{shy,i}$ (i=1,2,3,4,5) in *y*-direction can be calculated by equation (13), where $l_{sh,i}$ and $d_{sh,i}$ (i=1,2,3,4,5) are given in Table 3 and referred in Figure 9. k_{sh} is the thermal conductivity of the shaft.

$$R_{shy,i} = \frac{l_{sh,i}/2}{\pi\left(d_{sh,i}/2\right)^2 k_{sh}} = \frac{2l_{sh,i}}{\pi d_{sh,i}^2 k_{sh}} \qquad (13)$$

Similarly, the thermal resistance $R_{shz,i}$ (i=2,4,5) in *z*-direction in Figure 11 can be calculated by equation (14).

$$R_{shz,i} = \frac{d_{sh,i}/2}{\left(\pi d_{sh,i}/2\right) l_{sh,i} k_{sh}} \times \frac{1}{2} = \frac{1}{2\pi l_{sh,i} k_{sh}} \qquad (14)$$

The bearing thermal model is shown in Figure 12, in which R_{b1} and R_{b2} are the thermal resistances of the bearing 1 and bearing 2, respectively, including both conduction and convection ones.

The thermal models presented in Figure 8, Figure 10, Figure 11 and Figure 12 are combined into the model for the whole rotor in Figure 13. Here the mechanical losses in the two bearings are introduced as P_{b1} and P_{b2}. In Figure 13, R_{mr} is the contact thermal resistance between the magnets and the rotor iron, whilst R_{rsh} is the contact thermal resistance between the rotor iron and the shaft. Thermal resistances R_{rz}, R_{shl} and R_{shr} are introduced to simplify the shaft model presented in Figure 11:

$$\begin{cases} R_{rz} = 2R_{rz1} + 2R_{rz2} + R_{rz3} \\ R_{shl} = R_{shy4} + 2R_{shy3} + R_{shy2} + R_{shz2} \\ R_{shr} = R_{shy4} + R_{shy5} + R_{shz5} \end{cases} \tag{15}$$

3.2.4 Housing Thermal Model

The housing is modelled as 3 cylinders having an outer diameter $d_{ho,k}$ (k=1,2,3), an inner diameter $d_{hi,k}$ and a length $l_{h,k}$, respectively, as shown in Figure 9. These housing dimensions are listed in Table 3. The housing thermal model is shown in Figure 14. C_{h1}, C_{h2} and C_{h3} are the thermal capacities for the three cylinders, respectively, which can be obtained similar to the equation (6).

In Figure 14, the conduction thermal resistances $R_{hz,i}$ (i=1,3) in the z-direction can be given by equation (16), where $d_{ho,i}$, $d_{hi,i}$ and $l_{h,i}$ (i=1,3) can be referred in Table 3 and Figure 9. k_h is the thermal conductivity of the housing.

$$R_{hz,i} = \frac{d_{ho,i} - d_{hi,i}}{2\pi\left(d_{ho,i} + d_{hi,i}\right) l_{h,i} k_h} \tag{16}$$

The conduction thermal resistances R_{hy2} in the y-direction is obtained from equation (17), where d_{ho2}, d_{hi2} and l_{h2} can be referred in Table 3 and Figure 9.

$$R_{hy2} = \frac{2l_{h2}}{\pi(d_{ho2}^2 - d_{hi2}^2)k_h} \quad (17)$$

In Figure 14, R_{hsi} (i=1,2,3) are the thermal resistances between the housing surface and surrounding air, which is a combination of natural free thermal convection and radiation. This is calculated using equation (18) where h_{ci} and h_{ri} are the convection and radiation heat coefficients, respectively, of the surface s_i shown in Figure 9. S_i is the corresponding area for surface s_i.

$$R_{hsi} = \frac{1}{(h_{ci} + h_{ri})S_i} \quad (18)$$

The convective heat transfer coefficient is obtained from equation (19). In (19), Nu_i is the Nusselt number for the surface s_i, which is given in equation (20) [40] where the constant terms for different surfaces are provided in Table 4.

Table 4: Constants for natural convection correlations for motor housing external heat loss

	Surface		
	s_1	s_2	s_3
c_1	0.825	0.60	0.825
c_2	0.492	0.559	0.492

$$h_{ci} = Nu_i \frac{k_{air}}{d_{hoi}} \quad (19)$$

$$Nu_i = \left\{ c_1 + \frac{0.387 Ra_i^{1/6}}{[1 + (c_2/Pr_i)^{9/16}]^{8/27}} \right\}^2 \quad (20)$$

As for the surface s_i, the radiation heat coefficient h_{ri} is given by,

$$h_{ri} = \frac{q_{ri}}{T_{si} - T_a} = \frac{\varepsilon \sigma_c (T_{si}^4 - T_a^4)}{T_{si} - T_a} \quad (21)$$

where q_{ri} is the surface heat density for s_i. T_{si} is the surface temperature for s_i. ε is the emissivity coefficient for the housing material, e.g. Aluminium. σ_c is the Stefan-Boltzmann constant, i.e. 5.67 × 10^{-8} kg/s^{3}K^4.

3.2.5 Combined Thermal Model

By combining the thermal models shown in Figure 7, Figure 13 and Figure 14, the thermal model of the complete AFPM machine is shown in Figure 15. The assembly of the full motor model introduces two additional resistances: R_g is the convective thermal resistance of the airgap sandwiched by the stator and rotor; R_{hs} is the contact thermal resistance between the stator yoke and housing. The model parameters will be determined from experiments and FE analysis in section 4. In Figure 15, R_{h1} and R_{h2} are given by,

$$\begin{cases} R_{h1} = R_{hz1} + R_{hy2} \\ R_{h2} = R_{hz3} + R_{hy2} \end{cases} \tag{22}$$

The combined thermal model has been programmed in MATLAB/Simulink environment to measure the computational efficiency using a desktop PC application. The model was observed to run at just over 1000 times real time. This would easily allow for such a model to be included in propulsion system simulation codes in co-simulation with combustion engines and drivelines to predict overall system efficiencies over transient duty cycles. Equally, this is compatible with model-based architecture optimisation approaches which require physically based models to automatically identify system topologies. Finally, such a mathematical structure is a sensible starting point for further computational optimisation for on-board applications.

3.3 Experimental Setup

3.3.1 Test rigs

The motor was tested on an electric machine dynamometer as shown in Figure 16. The motor was powered by an external DC power supply using an ACD 4805 motor controller from Heinzmann. The

motor power was absorbed by the dynamometer system whilst measuring the output speed and torque. The AFPM test motor is tested to validate the results of the thermal models and the FE analysis. The goal of those measurements is to estimate the heat source in the AFPM, and the thermal behaviour of the AFPM itself. The accuracies and ranges of key sensors in Figure 16 are listed in Table 5. The load motor is a three-phase VASCAT induction machine with a rated speed 3266 rpm, a rated torque 220 Nm and a rated power 75.2 kW, of which the generated power is feedback to the electric grid via a AC-DC-AC converter.

As shown in Figure 16, a heat flow from the AFPM machine into the test rig through the housing cannot be neglected. However, this heat flow is extremely difficult to predict, due to the complex geometry of the test rig, and the unknown convective heat coefficient of the surface. Therefore, this thermal behaviour was rebuilt with two thermal RC elements as shown in Figure 15:

1. A first RC element is used for the rapid response of the mounting place (Resistance: R_{tr1}=0.95 K/W and Capacitance: C_{tr1}=3×10^4 J/K).
2. A second RC element represents the remainder of the rig with a much larger capacitance (Resistance: R_{tr2}=0.75 K/W and Capacitance: C_{tr2}=1×10^5 J/K).

The approach to find the right thermal resistances and thermal capacities is based on the curve fitting of the calorimetric measurement of the node temperature. In this calorimetric measurement, to determine the conduction taking place via the machine mounting and therefore calculate the thermal resistances and capacities of the motor mounting-test rig network, the thermal convection and thermal radiation from the AFPM machine surfaces is eliminated by lagging the machine with fibreglass wool. As the tuning of this parameter is empirical, both results with and without empirical tuning will be presented.

Table 5: Accuracies of Key Sensors

Sensor	Type	Range	Accuracy
Torque sensor	HBM T40B	-50 - 50 Nm	5%
Temperature sensor	K-type	-200 - 1260 °C	2°C
Current transducer	LEM IT 1000-S/SP1 ULTRASTAB	0 - 1000 A	0.0044 - 0.02725%
Voltage amplifier	Dewetron HSI-HV	0 – ±1400 V	0.05%

3.3.2 Test Motor Instrumentation

The AFPM itself was fitted with 13 K-Type thermocouples, as shown in Figure 17a. Thermocouples 1-10 are located on the housing and stator of the motor. Thermocouples 11-13 are located on the rotor itself and their readings transmitted via a wireless communication protocol to the data logger. All measurements of temperature were recorded at 1 Hz.

The wireless sensor system was a bespoke design for this research and was mounted onto the rotor as shown in Figure 17b [41].

The structure of the wireless sensor measurement for the AFPM machine is shown in Figure 18. As shown in Figure 18, there are three temperature sensors on the rotor. It is worth noting that these sensors should be capable to withstand temperatures of up to 100 °C and the centrifugal forces. These sensors should also be lightweight with a balanced mass distribution. To avoid using the error-prone slip-rings [36], [38] and prevent data distortion during transmission, all the signal outputs are digitized on the rotor, and sent continuously to the CAN-bus via the low pass filters on the rotor, as shown in Figure 18.

Battery based power supplies [42], [43] and slip ring unit [44] have been reported for the wireless rotor temperature measuring system for PM machines. However, battery-based power supplies need replacement and they are sensitive to high temperatures and mechanical vibrations, whilst the slip ring unit needs a regular maintenance and hence reduces the system stability and reliability. Here, an inductive power supply for these sensors are adopted, as shown in Figure 18. The inductive power supply consists of two coils, with the primary one fixed on the motor housing whilst the

secondary one fixed on the rotor, as shown in Figure 17b. To maximize the magnetic coupling and hence the power transmission between these two coils, the primary coil is partly inside the secondary coil [41]. As shown in Figure 17b, the secondary coil holder is made by plastic using a 3D printer to minimize its weight and to avoid a reverse magnetic flux within the area enclosed by the secondary windings.

The wireless sensor is based on a Preon32 radio module from Virtenio [45], programmed in C using the Contiki operating system [46].

3.3.3 Transient Model Validation Method

The thermal model was also tested over a generic transient cycle to assess the predictive capability during typical operating conditions. This validation has been conducted using a motor with an identical architecture, but with a larger frame size and a higher rated power (11 kW compared to 1.5 kW). The motor has been tested on the same experimental facility as described above. A reduced thermal instrumentation was installed on this motor, with only temperatures in the windings and on the front housing of the motor being recorded using k-type thermocouples.

To allow a direct comparison with the thermal model presented in this paper, the raw experimental results from this 11 kW motor have been scaled as follows:

- Motor speed is not scaled as both motors have the same speed range.
- Motor torque is scaled by a factor of 7.3 which represents the ratio of rated torque between the motors.
- Temperatures are not scaled as they are assumed to be similar in both machines.

The motor speed and torque during the transient test for this validation phase are shown in Figure 19a. The test was 10 minutes in duration and was constructed using swept frequency sine wave inputs, or chirp signals. The chirp signals excite the input between an upper and lower magnitude and upper and lower frequency (see Table 6). These are usually tailored for use cases, however as no

specific application was considered in this work, the frequency ranges were set the same for both speed and torque. Figure 19b shows the chirp signal on the motor's speed-torque map to illustrate that this intersects the continuous torque limit of the motor. The test cycle was repeated with two different motor start temperatures as measured in the windings of 25 °C and 50 °C.

Table 6: Excitation range and frequencies of the dynamic test cycle

	Magnitude		Frequency (Hz)	
	Upper	**Lower**	**Upper**	**Lower**
Speed (rpm)	2500	1000	0.125	0.008
Torque (Nm)	2	4.5	(8s period)	(120s period)

To use the thermal model, the thermal losses need to be estimated over the speed/torque region excited by the chirp test. As the losses have only been calculated individually at the rated condition (see section 4.2), a simple scaling approach has been adopted to estimate these losses at different speed and load conditions as follows:

- Bearing friction is scaled linearly with motor speed assuming zero loss at 0 rpm and the rated losses at 4500 rpm.
- Windage loss is proportional to the cube of motor speed, assuming zero loss at 0 rpm and the rated losses at 4500 rpm.
- Stator and rotor losses are scaled linearly with both motor torque and speed.
- Magnet loss is proportional to motor torque and to motor speed squared.
- Copper loss is proportional to motor torque squared.

4 MODEL PARAMETERIZATION

In this section, thermal resistances, capacitances and power losses in the LPTM is determined for the analysed 1.5 kW single side AFPM machine. Thermal resistances and capacitances are calculated based on the equations shown in section 3.2, whilst the losses are determined by the FE simulation.

A stationary DC test on the instrumented motor is conducted to assist determining the housing surface convective heat coefficient.

4.1 Thermal Resistances and Capacities

Based on the motor dimensional parameters shown in Table 3, the properties of motor parts shown in Table 7, the conduction thermal resistances and thermal capacities in the LPTM shown in Figure 15 are calculated and listed in Table 8. In this paper, the shaft material is assumed as the same as the rotor, i.e. AISI 1008 carbon steel. All the contact thermal resistances R_{mr}, R_{rsh} and R_{hs} are neglected, i.e. R_{mr}=R_{rsh}=R_{hs}=0, as well as the bearing conduction resistances R_{b1} and R_{b2}. It is worth noting that the thermal conductivity for the stator lamination M330-35A shown in Table 7 is only for the directions parallel to the lamination surface, i.e. *x*- and *y*-axis directions, not the *z*-axis direction. The thermal conductivity perpendicular to the plane is about 1/10 of that in plane [21]. It is also worth noting that the rotor is made by iron which is solid, not laminated or wound, hence in this paper the thermal conductivities of the rotor iron is set as isotropic with a thermal conductivity 60.5 W/mK (as shown in Table 7).

Table 7: Main Material Properties of Motor Parts

Material	Property	Value	Unit
Copper	Thermal conductivity, k_c	401	W/mK
	Specific heat, c_c	385	J/kgK
	Mass density, ρ_c	8950	Kg/m^3
	Electrical conductivity, σ_c	5.81	10^6s/m
Isolation	Thermal conductivity, k_i	0.13	W/mK
Resin	Thermal conductivity, k_r	1	W/mK
Liner: NOMEX	Thermal conductivity, k_l	0.13	W/mK
Stator iron: M330-35A	Thermal conductivity, k_{si}	25	W/mK
	Specific heat, c_{si}	490	J/kgK
	Mass density, ρ_{si}	7700	Kg/m^3
Rotor iron and shaft: Carbon Steel	Thermal conductivity, k_{ri}	60.5	W/mK
	Specific heat, c_{ri}	434	J/kgK
	Mass density, ρ_{ri}	7850	Kg/m^3
Magnet: N35UH	Thermal conductivity, k_m	6.75	W/mK
	Specific heat, c_m	460	J/kgK
	Mass density, ρ_m	7500	Kg/m^3
	Remanence flux density at 20°C, B_r	1.21	T
	Coercivity at 20°C, H_c	907	kA/m
	Temperature coefficient of B_r at 20°C, α_{Br}	-0.12	%
	Temperature coefficient of H_c at 20°C, α_{Hc}	-0.51	%
	Electrical conductivity, σ_{PM}	0.56	10^6s/m
Housing: Aluminium	Thermal conductivity, k_h	235	W/mK
	Specific heat, c_h	875	J/kgK
	Mass density, ρ_h	2770	Kg/m^3
	Electrical conductivity, σ_h	3.77	10^6s/m
Air	Thermal conductivity, k_{air}	0.0262	W/mK

The airgap convective thermal resistance (R_g) is obtained as follows: The Reynolds number for the disk geometry machine is given by equation (23) [47]. Based on the equation (23), the air-gap Reynolds number Re_g=9.77×10^4, when the rotor angular speed ω_r=4500 rpm and the air kinematic viscosity is taken as v_{air}=2×10^{-5} m^2/s. Since Re_g<2.8×10^5 [48], it is the laminar flow regime.

$$Re_g = \frac{\omega_r r_{r5}^2}{v_{air}} \qquad (23)$$

Based on Re_g obtained from the equation (23), as the ratio of the airgap height to the rotor radius is $G_g \approx 0.03$, the Nusselt number for the air-gap Nu_g can be given by (24) [49].

$$Nu_g = 0.5(1 + 5.47 \times 10^{-4} e^{112 G_g}) Re_g^{0.5} \qquad (24)$$

The airgap thermal convective heat coefficient h_g and convective thermal resistance R_g are calculated from equations (25) and (26).

$$h_g = \frac{Nu_g k_{air}}{r_{r5}} \quad (25)$$

$$R_g = \frac{1}{\pi(r_{r5}^2 - r_{r3}^2)h_g} \quad (26)$$

Based on equations (23)-(26), Nusselt number for the air-gap N_{ug}=158.63, air-gap thermal heat coefficient h_g=63.30 K/m^{2}W and air-gap convection thermal resistance R_g=1.66 K/W.

As shown in the equations (23) and (24), the Nusselt number for the airgap Nu_g is proportional to the square root of the rotor angular speed ω_r. Therefore, a larger Nusselt number for the airgap Nu_g and hence a better thermal dissipation capability through the air-gap can be obtained when the rotor speed is higher. If the rotor speed is larger to a transition or a turbulent flow turbulent flow, the thermal dissipation capability through the airgap will be even higher.

Table 8: Conduction Thermal Resistances (Unit: mK/W) and Thermal Capacities (Unit: J/K)

Symbol	Value	Symbol	Value	Symbol	Value
Winding	-	**Magnet**	-	**Shaft**	-
R_{lx}	8238.6	R_{my}	41.4762	R_{shy1}	1346.665
R_{ly}	17575.7	C_m	0.0132	R_{shy2}	420.9056
R_{cx}	11.1033	**Rotor iron**	-	R_{shy3}	233.8365
R_{cy}	58.1190	R_{ry3}	5.7743	R_{shy4}	328.3064
R_{ix}	4211.6	R_{rz1}	40.4717	R_{shy5}	407.7523
R_{iy}	22044.9	R_{rz2}	88.8497	R_{shz2}	164.4163
R_{rx}	3322.4	R_{rz3}	135.9672	R_{shz4}	134.9057
R_{ry}	17390.5	R_{rz4}	9.9641	R_{shz5}	169.7200
R_{cirx}	7545.1033	R_{rz}	394.6099	R_{shl}	1381.301
R_{ciry}	39493.519	C_r	326.6921	R_{shr}	905.7787
C_w	324.6606	**Housing**	-	C_{sh}	176.2151
Stator iron	-	R_{hy2}	15.1641	**Bearings**	-
R_{stx}	6.2608	R_{hz1}	0.8468	R_{b1}	0
R_{sty}	38.8980	R_{hz3}	43.0687	R_{b2}	0
R_{sby}	20.0940	C_{h1}	685.2992		
C_{st}	273.7654	C_{h2}	609.1548		
C_{sb}	252.5102	C_{h3}	485.8010		

4.2 Losses

The copper loss P_w of the analysed AFPM machine is given by (27). Here it is worth noting that P_w in the LPTM is not a constant but a function of temperature, as the phase winding copper resistivity increases with temperature. In (27), the coefficient R_{ac}/R_{dc} is applied to consider the AC copper loss. The AC loss consists of that due to skin effect and the proximity loss. Due to skin effect, the current density is the largest near the conductor surface but decreases exponentially with greater depths in the conductor. The conductor diameter d_c=0.67 mm is much smaller than the skin depth δ_{cu}=3.76 mm at 4500 rpm (electric frequency f_e=300 Hz), which can be calculated based on (28) [50]. The skin depth δ_{cu} is defined as the depth where the current density is 1/e (~36.8%) of the conductor surface value.

$$P_w = mI_{ph}^2 R_{ph} \frac{R_{ac}}{R_{dc}} \tag{27}$$

$$\delta_{cu} = \sqrt{\frac{1}{\pi \sigma_{cu} f_e \mu_0 \mu_{rcu}}} \tag{28}$$

where σ_{cu} is the electric conductivity of the copper conductor, μ_0 is vacuum permeability, μ_{rcu} is the relative permeability of the copper winding.

Based on the equation (29), the ratio of the AC resistance to the DC resistance can be obtained as R_{ac}/R_{dc}=1.061. The proximity copper loss can be obtained by using the widely used 1-D analytical model shown in (30) [51], of which the order of magnitude is 10^{-10} W at 300 Hz, hence it can be neglected. In (30), l_{active} is the active length, B_m is peak flux density.

$$\begin{aligned} \frac{R_{ac}}{R_{dc}} &= \frac{\pi d_c^2}{4\int_0^{2\pi}\int_0^{\frac{d_c}{2}} e^{-\frac{r}{\delta_{cu}}} r dr d\theta} \\ &= \frac{d_c^2}{8\delta_{cu}^2\left[e^{-\frac{d_c}{2\delta_{cu}}}\left(-\frac{d_c}{2\delta_{cu}}-1\right)+1\right]} \end{aligned} \tag{29}$$

$$P_{px} = \frac{\pi}{16} l_{active} d_c^4 B_m^2 f_e^2 \tag{30}$$

With consideration of the hysteresis loss component and eddy current loss component, but neglecting the excess loss component, the iron loss P_{fe} of the analysed AFPM machine can be given by [52],

$$P_{fe} = k_{hl} f_e B_m^2 + k_{cl} f_e^2 B_m^2 \qquad (31)$$

where k_{hl} and k_{cl} are the hysteresis loss coefficient and eddy current loss coefficient, respectively. f_e and B_m are the electric frequency and amplitude of flux density, respectively.

The magnet eddy current loss P_m can be calculated by equation (32), in which σ_{PM} is the electric conductivity of PM, $\boldsymbol{J}_{PM}$ is the PM eddy current density and V_{PM} is the PM volume. It is worth noting that hysteresis loss component of the iron loss is proportional to the electric frequency and hence the rotor speed, whilst the eddy currents loss component is proportional to the square of the rotor speed, as shown in the equation (31). Similarly, the PM eddy current density $\boldsymbol{J}_{PM}$ shown in (32) is also proportional to the square of the rotor speed. Therefore, the hysteresis loss component and the eddy currents loss component of iron loss and PM eddy currents loss at one specific speed can lead to those losses at other speeds as long as the electromagnetic condition is the same, i.e. both the phase current amplitude and phase advanced angle are the same.

$$P_m = \frac{1}{\sigma_{PM}} \int \boldsymbol{J}_{PM}^2 dV_{PM} \qquad (32)$$

The mechanical loss P_{mech} can be generally separated in friction losses P_{b1} and P_{b2} in the bearing and windage losses P_{wd} [17],

$$\begin{cases} P_{mech} = p_{b1} + p_{b2} + p_{wd} \\ P_{b1} = P_{b2} = 0.06 k_{fb} (m_r + m_{sh}) \Omega \\ P_{wd} = 4 c_f \rho_{cm} \pi^3 \Omega^3 (R_{r5}^5 - R_{sh5}^5) \end{cases} \qquad (33)$$

where k_{fb}=1.5 - 3 m^2/s^2. m_r and m_{sh} are the mass of the rotor and the shaft, respectively. c_f=0.011 is the drag coefficient. ρ_{cm}=1.2 kg/m^3 is the specific density of the cooling medium. R_{sh5}=10 mm is the outer radius of the shaft.

Based on equations (27)-(33), the loss components and the total loss can be obtained, as listed in Table 9. Based on equation (34), the rated efficiency η_n is 91%, which is only 1% higher than that provided by the manufacturer shown in Table 2.

$$\eta_n = \frac{P_{out}}{P_{in}} \times 100\% = \frac{P_n}{P_n + p_{loss}} \times 100\% \qquad (34)$$

Table 9: Losses at Rated Condition of the Analyzed AFPM Machine

Item	Value	Unit
Copper loss at 20°C, P_w	99.77	W
3-D FEA predicted stator iron loss, P_{si}	38.60	W
3-D FEA predicted rotor iron loss, P_{ri}	2.55	W
3-D FEA predicted PM eddy current loss, P_m	3.78	W
Bearing 1 friction loss, P_{b1}	2.90	W
Bearing 2 friction loss, P_{b2}	2.90	W
Windage losses, P_{wd}	0.62	W
Total loss, P_{loss}	151.12	W

4.3 Thermal Analysis with FE

4.3.1 Calorimetric Measurement

Figure 20a shows the corresponding FE simulation for the DC test with I_{dc}=30 A, in which the copper loss is P_w=57.56 W, resulting in a heat flux in the slots 2269 W/m^2 and the convective heat coefficient of the whole housing surface is set as h_{cavg}=7.8 W/m^{2}K (based on the DC test experimental measurements shown later in section 5.1). As shown in Figure 20a, the temperature difference between the hottest and coldest part in the AFPM machine is about 11K at steady state condition. As a result, the thermal resistance from the slots to the housing can be calculated as 0.2 K/W. Therefore, a large difference for rated conditions is not expected. However, for more extreme operation points, e.g. very short high torque operations the thermal capacities will dominate the

behaviour. It is worth noting that the windings are not part of this simulation and this is discussed in the following section.

4.3.2 Influence of Thermal Conductivities of Resin and Liner

Since an accurate model of the slot is a complex problem, here an FE analysis is conducted to predict the thermal distribution inside the slot. The aim is to derive the behaviour for different materials inside the slot, including copper, isolation, resin and liner. A widely used material for the liner is NOMEX with a thermal conductivity of k_l=0.13 W/mK. Figure 20b shows the result of a thermal analysis (k_r=1 W/mK, k_l=0.13 W/mK) for the slot. Here, the boundaries are 0 °C, and the heat generation in the slots is set to 1938.2 kW/m^3. Due to the fact that the exact position of the windings is more or less random in the real AFPM machine, this captures just one of the solutions. As the material of the resin is unknown, the simulation was also conducted for several different thermal conductivities for the resin as well as for the liner.

Figure 21 shows the maximum temperature of the slot for different thermal conductivities of the resin and liner. The maximum temperature exhibits a non-linear increase as liner conductivity decreases. Due to the non-perfect manufacturing process in a real motor, there is always a small airgap between the tooth and the liner, which will decrease the effective conductivity. Furthermore, the effect of a resin conductivity is negligible once greater than 0.4 W/mK.

5 EXPERIMENTAL VALIDATION

5.1 DC Current Thermal Test

Here the AFPM machine is fed with a constant DC current for about 8-hour to achieve a steady state to measure and calibrate the convective thermal coefficient of the housing. During the DC test, the only power loss is the copper loss of two-phase windings which are injected by a DC current I_{dc}. Here a mean value h_{cavg} is measured for the whole housing surface,

$$h_{cavg} = \frac{P_w}{S_h\left(T_{savg} - T_a\right)} = \frac{2I_{dc}^2 R_{ph}}{S_h\left(T_{savg} - T_a\right)} \qquad (35)$$

where T_{savg} is the average temperature of the housing surface. S_h is the whole housing surface area.

According to equation (35) and Table 10, when the phase winding DC current I_{dc}=30 A, the steady state average convective thermal coefficient of the housing surface can be calculated as h_{cavg}=7.8 W/m^{2}K. It is worth noting that in the DC current thermal test, the AFPM machine is thermally isolated from the test rig, i.e. the only thermal dissipation path of the AFPM machine is via the housing surface. It is also worth noting that in the DC current thermal test, the only loss of the AFPM machine is two phase windings copper loss, which is 40.77W at ambient temperature. Compared with the total loss at the rated condition 145.38W, this copper loss is small, leading to a long time (~8 hours) to reach steady-state.

Table 10: Parameters for Calculating Housing Surface Average Convective Thermal Coefficient

Item	value	Unit
Phase winding DC current, I_{dc}	30	A
Phase winding resistance at 20°C, R_{ph}	22.65	mΩ
Copper resistance temperature coefficient at 20°C, α_c	4.3	10^{-3}/°C
Winding temperature, T_w	116	°C
Average temperature of the housing surface, T_{savg}	90.28	°C
Ambient temperature, T_a	22.35	°C

5.2 Steady State Thermal Validation

Figure 22 shows the comparison of the temperatures of thermocouples T_1, T_2, T_3 and T_7 between the LPTM and the measurements. As shown in Figure 22 and Table 11, the temperatures predicted by the LPTM are 30 °C ~ 40 °C smaller than the measurements. The principal explanation is that the calculated convective heat coefficient h_{cavg}=5.3 W/m^{2}K is underestimated in the LPTM. However, if the measured convective heat coefficient h_{cavg}=7.8 W/m^{2}K from the DC test is employed in the LPTM, the error will be reduced to <4 °C, as shown in Figure 22 and Table 11. As a result, the thermal convective coefficient has a big impact and has to be measured very precisely in the DC test.

In Table 1 it was shown that other models proposed in the literature with a similar number of nodes achieved a maximum absolute steady state prediction error of 3 °C to 4°C. It should be noted that this maximum error occurred in the windings, whilst in this paper the prediction error for the windings is 1.95 °C, as can be seen from Table 11. This 4 °C error is smaller than that of the LPTM for the interior PM (IPM) machine proposed in [37] (magnet temperature error of 5 °C) and that for the PM assisted synchronous reluctance machine (PMsSynRM) in [38] (winding temperature error of 10 °C).

Table 11: Comparison of Temperatures of Thermocouples T_1, T_2, T_3 and T_7 between LPTM and Measurement under Steady State

Thermocouple	Locations	Measurement (°C)	LPTM 1 (°C)	Error (°C)	Error (%, K/K)	LPTM 2 (°C)	Error (°C)	Error (%, K/K)
T_1	Stator tooth	98.50	131.38	-32.88	-8.85	95.47	-3.03	-0.82
T_2	Stator back	94.50	125.89	-31.39	-8.54	90.50	-4.00	-1.09
T_3	Housing	90.00	124.67	-34.67	-9.55	89.39	-0.61	-0.17
T_7	Winding	112.00	151.82	-39.82	-10.34	113.95	1.95	0.51

5.3 Simple Transient State Thermal Validation

As compared in Appendix, the measured loss for the rated operation point, i.e. T_{outn}=3.18 Nm and Ω_n=4500 rpm, is 152.76W, which is 1.1% higher than the calculated total loss shown in Table 9, i.e. 151.12W. This validates the effectiveness of the loss calculation shown in sub-section 4.2.

In the transient thermal test, the AFPM machine is directly coupled to the test bench shown in Figure 16. The AFPM machine was operating at rated condition (T_{outn}=3.18 Nm and Ω_n=4500 rpm) for the first 43 minutes at which time the motor power supply was switched off. The transient thermal test lasts for 120 minutes in total, of which the tested duty cycle including shaft speed and shaft torque are shown in Figure 23(a). Figure 23(b) to Figure 23(g) show a comparison of measured and LPTM predicted temperatures with and without consideration of the heat flow to the test rig. The impact of the heat flow into the rig is not negligible. Moreover, the temperature curves predicted by LPTM with consideration of the heat flow to the test rig agree well with those measured ones. However, there is still a significant difference in rising temperature curve, as captured in the

maximum temperature errors in Table 12. One reason could be the impact of the airgap thermal resistance, which was calculated on empirical equations with a simplified geometry.

As shown in Table 1, there is little data quantifying the accuracy of LPTM models under transient conditions. The maximum error observed in this work under transients is 13.5°C which is smaller than that of the radial flux surface-mounted PM (SPM) machine model proposed in [36] (20°C) and that of the radial flux SPM machine without rotor sleeve in proposed in [30] (25°C). Although the transient-state maximum absolute prediction error of the LPTM for the SPM machine without rotor sleeve proposed in [35] is only ~10°C for the shaft, this model is composed of 35 thermal nodes compared to 10 for the model proposed in this paper.

Table 12: Comparison of Temperatures of Thermocouples T_1, T_2, T_3, T_7, T_{12} and T_{13} between LPTM and Measurement under Transient State (Unit: °C)

Thermocouple	Location	Mean absolute error (0 – 43 min)	Max. absolute error (0 – 43 min)	Mean absolute error (44 min – 120 min)	Max. absolute error (44 min – 120 min)
T_1	Stator tooth	-1.52	9.53	-5.56	6.10
T_2	Stator back	-2.55	5.83	-5.17	4.58
T_3	Housing	-4.36	3.33	-5.79	2.89
T_7	Winding	2.94	13.45	-8.70	-0.37
T_{12}	Magnet	-3.04	4.04	-0.25	4.36
T_{13}	Rotor iron	-10.83	-0.76	2.09	6.57

Figure 24 shows the influence of R_g on the PM temperature predicted by LPTM, together with the measured results, in which R_g=9.01 K/W for the pure air conduction without convection. As shown in Figure 24, a smaller R_g may improve the accuracy of the LPTM. Since the heat flow is flowing from the stator to the PMs, the PM temperature is rising leading a better thermal convection inside the airgap.

5.4 Chirp Transient Validation

The comparison for the modelled and measured motor winding and housing temperatures during the transient chip tests are shown in Figure 25. The maximum and mean errors are presented in

Table 13. All errors in these transient test cycles are similar in magnitude to those reported for the step change tests in section 5.3. The maximum error is 4 °C which occurs in the windings during the 25 °C start test (see Figure 25b). Overall the prediction for the 50 °C start test (Figure 25a) is superior that that for the 25°C start test. Both tests clearly show an overall increase in temperature over the 10 minutes cycle which shows that the motor has not reached a state of fully warm operation. Even so, the model captures well the dynamics of the winding temperature due to the changes in motor speed and load. This is especially visible between 100s and 300s. The response of the housing temperature is much damped oozing to the thermal capacitances within the system. This is a promising result for the predictive power of the model as it has been applied scaled data.

Table 13: Maximum and mean errors during 25 °C and 50 °C chirp transient test for windings and motor housing (Unit: °C)

		50 °C Start	25 °C Start
Windings	*Maximum*	3.26	3.58
	Mean	0.78	1.70
Housing	*Maximum*	1.74	1.13
	Mean	1.12	0.51

6 CONCLUSION

In this paper, the methodology for characterizing the thermal behaviour of all the components in the single sided AFPM machine is presented. The contact temperature measurement on the rotor is applied for the first time in AFPM machines to demonstrate the ability of the LPTM to predict all component temperatures with an error $<$4 °C for steady state. During transients, the mean temperature error was 5 °C with a maximum error of 13.5 °C which was seen for the winding. The approach is shown to be accurate in transient conditions whilst retaining a low computational load. The approach is exemplified for a 1.5 kW 24-slot/8-pole air cooled motor and validated by experimental measurements. The proposed LPTM can be used within system simulations during the design process and/or embedded in controllers of the full powertrain, to avoid over-designing of the

powertrains, vehicles and achieve more accurate model-based control strategies accounting the thermal behaviour.

Two recommendations for designing such LPTM are given as follows.

1) It is found that there is a significant impact of the housing surface convective heat coefficient on the steady-state temperature predicted by LPTM, and hence the calorimetric measurements based on the DC current test need to be conducted as precisely as possible.

2) It is also found that the heat flow from the AFPM machine to the test rig through the housing cannot be neglected. Good agreements can also be achieved if the thermal model of the test rig is accounted for as two thermal RC elements in the LPTM.

7 APPENDIX

Based on the test bench shown in Figure 16, the efficiency map of the AFPM test motor is shown in Figure 26. As shown in Figure 26, the efficiency is about 90% for the rated operation point, which is laying in the best efficiently area. The only operation point which can be directly verified is for the rated condition, i.e. T_{outn}=3.18 Nm and Ω_n=4500 rpm. The rated efficiency error between the measurements and the manufacturer data is 0.9%, as shown in Table 14. For this operation point power losses of P_{loss}=152.75 W, which is slightly higher than that estimated in FE simulation (Table 9). The measured loss for the rated operation point is 152.76W, which is 1.1% higher than the calculated total loss shown in Table 9, i.e. 151.12W.

Table 14: Comparison of AFPM Machine Specifications between Datasheet and Measurement

Item	Unit	Datasheet	Measurement	Error
Winding inductance, L_{ph}	μH	107.0	111.0	3.6%
Line-line RMS back-EMF constant, K_{be}	V / 1000 rpm	5.79	5.89	1.4%
Rated line-line RMS voltage, U_{lln}	V	33.6	35.8	6.1%
Rated output mechanical power, P_{outn}	W	1500	1489.8	-0.7%
Rated output mechanical torque, T_{outn}	Nm	3.18	3.16	-0.6%
Rated line RMS current, I_{ln}	A	37.2	37.4	0.5%
Rated efficiency, η_n	%	89.9	90.7	0.9%

8 REFERENCES

[1] Z. Q. Zhu and D. Howe, “Electrical machines and drives for electric, hybrid and fuel cell vehicles,” *Proc. IEEE*, vol. 95, no. 4, pp. 746–765, Apr. 2007.

[2] M. Ehsani, Y. Gao, and J. M. Miller, “Hybrid electric vehicles: Architecture and motor drives,” *Proc. IEEE*, vol. 95, no. 4, pp. 719-728, Apr. 2007.

[3] T. A. Burress *et al.*, “Evaluation of the 2010 Toyota Prius hybrid synergy drive system,” Oak Ridge Nat. Lab., Oak Ridge, TN, USA, Rep. ORNL/TM2010/253, 2011.

[4] T. J. Woolmer and M. D. McCulloch, “Analysis of the yokeless and segmented armature machine,” *in Proc. of IEMDC2007*, Antalya, Turkey, May 2007, pp. 704-708.

[5] R. Camilleri, T. Woolmer, A. Court, and M. D. McCulloch, “Investigation into the temperature profile of a liquid cooled YASA© AFPM machine,” *in Proc. of PEMD2012*, Bristol, Mar. 2012, pp. 1–8.

[6] C. Liao, C. Chen, and T. Katcher, “Thermal analysis for design of high performance motors,” *in Proc. 6th ITHERM*, 1998, pp. 424–433.

[7] G. Moreno, S. Narumanchi, K. Bennion, S. Waye, and D. DeVoto, “Gaining traction: thermal management and reliability of automotive electric traction-drive systems,” *IEEE Electri. Mag.*, vol. 2, no. 2, pp. 42–49, Jun. 2014.

[8] J. Dalby, F. Fiquet, A. Ward, H. Stoffels, et al. “Hybrid powertrain technology assessment through an integrated simulation approach,” *in Proc. of 14th International Conference on Engines & Vehicles*, Aachen, Germany, 2019, Art. ID 2019-24-0167.

[9] D. Zhang, X. Zeng, P. Wang, and Q. Wang, “Co-simulation with AMESim and MATLAB for differential dynamic coupling of hybrid electric vehicle,” *2009 IEEE Intelligent Vehicles Symposium*, Xi'an, China, 2009, pp. 761–765.

[10] M. A. Ahmad, I. Baba, S. Azuma, and T. Sugie, “Model free tuning of variable state of charge target of hybrid electric vehicles,” *IFAC Proc. Vol.*, vol. 46, no. 21, pp. 789–793, 2013.

[11]N. P. Shah, A. D. Hirzel, and B. Cho, “Transmissionless selectively aligned surface-permanent-magnet BLDC motor in hybrid electric vehicles,” *IEEE Trans. Ind. Electron.*, vol. 57, no. 2, pp. 669–677, Feb. 2010.

[12]S. A. Anbaran, N. R. N. Idris, M. Jannati, M. J. Aziz, and I. Alsofyani, “Rule-based supervisory control of split-parallel hybrid electric vehicle,” *2014 IEEE Conference on Energy Conversion (CENCON)*, Johor Bahru, Malaysia, 2014, pp. 7–12.

[13]A. Hughes and W. Drury, *Electric Motors and Drives – Fundamentals, Types and Applications, 4th Edition*. Elsevier, Oxford, UK, 2013, pp. 19–22.

[14]Y. Wang, X. Wen, C. Chen, Y. Li, and L. Xu, “Peak power improvement of interior permanent motor for electrified ,” *IEEE Electri. Mag.*, vol. 2, no. 2, pp. 25–30, Jun. 2014.

[15]Y. Huang, H. Wang, A. Khajepour, H. He, and J. Ji, “Model predictive control power management strategies for HEVs: a review,” *Journal of Power Sources*, vol. 341, pp. 91–106, Feb. 2017.

[16]M. Aydin, S. Huang, and T. A. Lipo, “Axial flux permanent magnet disc machines: A review,” in *Proc. of SPEEDAM*, Jun. 2004, pp. 61–71.

[17]J. F. Gieras, R.-J. Wang, M. J. Kamper. *Axial Flux Permanent Magnet Brushless Machines*, 2nd ed. Springer, 2008.

[18]F. G. Capponi, G. D. Donato, and F. Caricchi, “Recent advances in axial-flux permanent-magnet machine technology,” *IEEE Trans. Ind. Appl.*, vol. 48, no. 6, pp. 2190–2205, Nov./Dec. 2012.

[19]A. M. Cascio, “Modeling, analysis and testing of orthotropic stator structures,” *in Proc. of Naval Symp. on Electr. Mach.*, Newport, US, 1997, pp. 91–99.

[20]E. Spooner and B. J. Chalmers, “TORUS’; A slotless, toroidal-stator, permanent-magnet generator,” *IEE Proc.-B*, vol. 139, no. 6, pp. 497–506, Nov. 1992.

[21]N. Rostami, M. R. Feyzi, J. Pyrhonen, A. Parviainen, and M. Niemela, “Lumped-parameter thermal model for axial flux permanent magnet machines,” *IEEE Trans. Magn.*, vol. 49, no. 3, pp. 1178–1184, Mar. 2013.

[22]F. Marignetti, V. Delli Colli, and Y. Coia, “Design of axial flux PM synchronous machines through 3-D coupled electromagnetic thermal and fluid-dynamical finite-element analysis,” *IEEE Trans. Ind. Electron.*, vol. 55, no. 10, pp. 3591–3601, Oct. 2008.

[23]A. Rasekh, P. Sergeant, and J. Vierendeels, “Convective heat transfer prediction in disk-type electrical machines,” *Applied Thermal Engineering*, vol. 91, pp. 778–790, Dec. 2015.

[24]A. Boglietti, A. Cavagnino, D. Staton, M. Shanel, M. Mueller, and C. Mejuto, “Evolution and modern approaches for thermal analysis of electrical machines,” *IEEE Trans. Ind. Electron.*, vol. 56, no. 3, pp. 871–882, Mar. 2009.

[25]K. Zhou, J. Pries, and H. Hofmann, “Computationally efficient 3-D finite-element-based dynamic thermal models of electric machines,” *IEEE Trans. Veh. Tech.*, vol. 1, no. 2, pp. 138–149, Aug. 2015.

[26]R. Wrobel, G. Vainel, C. Copeland, T. Duda, D. Staton, and P. H. Mellor, “Investigation of mechanical loss components and heat transfer in an axial-flux PM machine,” *IEEE Trans. Ind. Appl.*, vol. 51, no. 4, pp. 3000–3011, Jul./Aug. 2015.

[27]R. Wrobel and P. H. Mellor, “A general cuboidal element for three-dimensional thermal modelling,” *IEEE Trans. Magn.*, vol. 46, no. 8, pp. 3197–3200, Aug. 2010.

[28]F. Marignetti and V. Delli Colli, “Thermal analysis of an axial flux permanent-magnet synchronous machine,” *IEEE Trans. Magn.*, vol. 45, no. 7, pp. 2970–2975, Jul. 2009.

[29]Z. W. Vilar, D. Patterson, and R. A. Dougal, “Thermal analysis of a single sided axial flux permanent magnet motor,” *in Proc. of IECON2005*, Raleigh, US, Nov. 2005, pp. 5 pp. 2570–2574.

[30]J. Hey, D. A. Howey, R. Martinez-Botas, and M. Lamperth, “Transient thermal modelling of an axial flux permanent magnet (AFPM) machine with model parameter optimisation using a Monte Carlo method,” *in Proc.* VTMS10, Warwickshire, UK, 2011.

[31]A. H. R. Mohamed, H. Vansompel, A. Hemeida, and P. Sergeant, “Transient lumped parameter thermal model *based* loadability studies for the YASA axial flux permanent magnet synchronous machines,” in Young Researchers Symposium, Brussels, 2018.

[32]E. Belicova and V. Hrabovcova, “Analysis of an axial flux permanent magnet machine (AFPM) based on coupling of two separated simulation models (electrical and thermal ones),” *Journal of Elec. Eng.*, vol. 58, no. 1, pp. 3–9, Mar. 2007.

[33]G. Vainel, D. A. Staton, F. G. Capponi, G. Donato, and F. Caricchi, “Thermal modelling of a fractional-slot concentrated-winding Kaman type axial-flux permanent-magnet machine,” *in Proc.* ECCE2013, Denver, USA, 2013, pp. 1505–1511.

[34]A. Kačenka, A. Pop, I. Vintiloiu, and D. Fodorean, “Lumped parameter thermal modeling of permanent magnet synchronous motor,” *in Proc. of* 2019 Electric Vehicles International Conference (EV), Bucharest, Romania, 2019, pp. 1–6.

[35]D. G. Dorrell, “Combined thermal and electromagnetic analysis of permanent-magnet and induction machines to aid calculation,” *IEEE Trans. Ind. Electron.*, vol. 55, no. 10, pp. 3566–3574, Oct. 2008.

[36]N. Zhao and W. Liu, “Loss calculation and thermal analysis of surface-mounted PM motor and interior PM motor,” *IEEE Trans. Magn.*, vol. 51, no. 11, pp. 1–4, Nov. 2015, Art. ID 8112604.

[37]P. Mellor, R. Wrobel, A. Mlot, T. Horseman, and D. Staton, “Influence of winding design on losses in brushless AC IPM propulsion motors,” *in Proc. of ECCE*2011, Phoenix, US, 2011, pp. 2782–2789.

[38]S. Nategh, O. Wallmark, M. Leksell, and S. Zhao, “Thermal analysis of a PMaSRM using partial FEA and lumped parameter modeling,” *IEEE Trans. Energy Conv.*, vol. 27, no. 2, pp. 477–488, Jun. 2012.

[39]D. Staton, A. Boglietti, and A. Cavagnino, “Solving the more difficult aspects of electric motor thermal analysis in small and medium size industrial induction motors,” *IEEE Trans. Energy Convers.*, vol. 20, no. 3, pp. 620–628, Sep. 2005.

[40]M. Markovic, L. Saunders, and Y. Perriard, “Determination of the thermal convection coefficient for a small electric motor,” *in Conf. Rec. of 41st IAS Annual Meeting*, Tampa, US, 2006, pp. 58–61.

[41]A. Bock, D. Liu, J. Funck, A. Giedymin, R. Burke, and C. Gühmann, “Wireless sensor for temperature and flux measurements in an axial flux machine,” in *Proc. AMA Conferences 2015*, Nürnberg, Germany, May 2015, pp. 361–366.

[42]D. D. Reigosa, D. Fernandez, H. Yoshida, T. Kato, and F. Briz, “Permanent-magnet temperature estimation in PMSMs using pulsating high-frequency current injection,” *IEEE Trans. Ind. Appl.*, vol. 51, no. 4, pp. 3159–3168, Jul.-Aug. 2015.

[43]D. Park, H. Jung, H. Cho, and S. Sul, “Design of wireless temperature monitoring system for measurement of magnet temperature of IPMSM,” *in Proc. ITEC2018*, Long Beach, US, 2018, pp. 656–661.

[44]C. Du-Bar, J. Aström, T. Thiringer, S. Lundmark, and M. Alatalo, “Design of an online temperature monitoring system for an experimental IPMSM,” *in Proc.* ICEM2016, Lausanne, Switzerland, 2016, pp. 1533–1538.

[45]https://www.virtenio.com/en/portfolio-items/preon32/, accessed on 30th January 2020.

[46]http://www.contiki-os.org/, accessed on 30th January 2020.

[47]D. A. Howey, P. R. N. Childs, and A. S. Holmes, “Air-gap convection in rotating electrical machines,” *IEEE Trans. Ind. Appl.*, vol. 59, no. 3, pp. 1367–1375, Mar. 2012.

[48]J. M. Owen, C. M. Haynes, and F. J. Bayley, “Heat transfer from an air-cooled rotating disk,” *Proc. R. Soc. Lond. A*, *Math. Phys. Sci.*, vol. 336, pp. 453–473, Feb. 1974.

[49]R. Boutarfa and S. Harmand, “Local convective heat transfer for laminar and turbulent flow in a rotor-stator system,” *Experiments in Fluids*, vol. 38, no. 2, pp. 209–221, Feb. 2005.

[50]W. C. Johnson. *Transmission Lines and Networks*. McGraw-Hill, 1950.

[51]C. R. Sullivan, "Computationally efficient winding loss calculation with multiple windings, arbitrary waveforms, and two-dimensional or three-dimensional field geometry," *IEEE Trans. Power Electro.*, vol. 16, no. 1, pp. 142–150, Jan. 2001.

[52]H. Domeki *et al.*, "Investigation of benchmark model for estimating iron loss in rotating machine," *IEEE Trans. Magn*., vol. 40, no. 2, pp. 794–797, Mar. 2004.

9 NOMENCLATURE

A_m	Surface area of each PM
A_{sam}	Cross-section area of the sample
B_m	Amplitude of flux density
c_f	Drag coefficient
C_{hi} (i=1,2,3)	Thermal capacities for the housing cylinder i
C_m	Thermal capacity of PMs
C_r	Thermal capacity of rotor iron
C_{ri} (i=1,2,3,4)	Thermal capacity of the four rotor iron part i
C_{sb}	Thermal capacity of stator back
C_{sh}	Thermal capacity of shaft
C_{st}	Thermal capacity of stator tooth
C_w	Thermal capacity of winding
$C_{w,slot}$	Thermal capacity of winding in individual slot
c_w, c_{si}, c_m	Specific heat capacity of winding, stator iron, magnets
d_c	Conductor diameter
f_c, f_r, f_i	Effective filling factor for copper winding, resin, isolation
f_e	Electric frequency
h_{cavg}	Average convection heat coefficient of whole housing surface
h_{ci} (i=1,2,3)	Convection heat coefficient for housing surface cylinder i
H_m	Height of each PM
h_{ri} (i=1,2,3)	Radiation heat coefficient of housing surface cylinder i
H_{sb}, W_{sb}, L_{sb}	Height, width and length of the stator back
H_{st}, W_{st}, L_{st}	Stator tooth height, width, length
I_{ln}	Rated line RMS current
I_{ph}	Phase winding current RMS value
I_{phn}	Rated phase winding RMS current
J_{PM}	PM eddy current
k_{air}	Thermal conductivity of air
k_c	Thermal conductivity of copper winding

k_h	Thermal conductivity of housing
k_{hl}, k_{cl}	Hysteresis and eddy current loss coefficients
k_i	Thermal conductivity of isolation
k_l	Thermal conductivity of liner
k_m	Thermal conductivity of magnets
k_r	Thermal conductivity of resin
k_{ri}	Thermal conductivity of rotor iron
k_{sam}	Thermal conductivity of the sample
k_{sh}	Thermal conductivity of shaft
k_{si}	Thermal conductivity of stator iron
l_{active}	Active length of the machine
L_s, H_s, W_s	Stator slot length, height, width
m	Phase number
m_r	Rotor mass
m_{ri} (i=1,2,3,4)	Mass of rotor iron part i
m_{sh}	Shaft mass
m_w	Mass of winding
Nu_i, Ra_i, Pr_i	Nusselt number, Rayleigh number, Prandtl number of surface S_i
p	Rotor pole-pair number
P_{b1}, P_{b2}	Bearing friction loss of bearing 1, 2
P_{fe}	Iron loss
P_{in}	Input electric power
P_{loss}	Total loss
P_m	Magnet eddy current loss
P_{mech}	Mechanical loss
P_n	Rated electromagnetic power
P_{out}	Output mechanical power
P_{px}	Proximity copper loss
P_{ri}	Rotor iron loss
P_{si}	Stator iron loss
P_w	Winding copper loss
$P_{w,slot}$	Individual slot winding copper loss
P_{wd}	Windage losses
Q	Stator slot number
$q_{r,i}$ (i=1,2,3)	Surface heat density for housing surface S_i
R_{b1}, R_{b2}	Thermal resistances of the bearing 1, 2
R_{cx}, R_{cy}	Thermal resistances of winding in x-, y-direction
R_g	Convective thermal resistance of the air-gap
R_{hs}	Contact thermal resistance between stator yoke and housing
R_{hsi} (i=1,2,3)	Thermal resistance between the housing surface i and surrounding air
R_{hy2}	Conduction thermal resistances between bearing and house cylinder 2 in y-direction

$R_{hz,i}$ (i=1,3)	Conduction thermal resistances between bearing and house cylinder i in z-direction
R_{ix}, R_{iy}	Thermal resistance of isolation in x-, y-direction
R_{mr}	Contact thermal resistance between PMs and rotor iron
R_{my}	Thermal resistance of PMs in y-direction
R_{ph}	Phase winding electric resistance
R_{rsh}	Contact thermal resistance between rotor iron and shaft
R_{rx}, R_{ry}	Thermal resistance of resin in x-, y-direction
R_{ry3}	Thermal resistance in y-direction of the rotor iron part 3
R_{rzi} (i=1,2,3,4)	Thermal resistance of rotor iron part i in z-direction
R_{sam}	Thermal resistance across the thickness of the sample
R_{sby}	Thermal resistance of stator back in y-direction
R_{shxi} (i=1,2,3,4,5)	Thermal resistances of shaft part i in x-direction
$R_{shy,i}$ (i=1,2,3,4,5)	Thermal resistances of shaft part i in y-direction
R_{shzi} (i=1,2,3,4, 5)	Thermal resistances in z-direction of the five shaft parts from left to right
R_{stx}, R_{sty}	Thermal resistance of stator tooth in x-, y-direction
S_h	Whole area of housing surfaces
S_i (i=1,2,3)	Area for housing surface s_i
T_a	Ambient temperature
T_{out}	Output mechanical torque
T_{savg}	Average temperature of the housing surface
T_{si} (i=1,2,3)	Temperature for housing surface s_i
U_{phn}	Rated phase winding RMS voltage
V_{PM}	PM volume
W_l	Stator liner width
α_{air}	Air thermal diffusivity
β_{air}	Air expansions coefficient
Δx_{sam}	Thickness of the sample
ε	Emissivity coefficient for the housing material
η_n	Rated efficiency
μ_0	Vacuum permeability
μ_{rcu}	Relative permeability of the copper winding
ρ_{cm}	Mass density of cooling medium for bearing
ρ_r	Mass density of rotor iron
σ_c	Stefan-Boltzmann constant
σ_{cu}	Electric conductivity of the copper conductor
σ_{PM}	Electric conductivity of the PMs

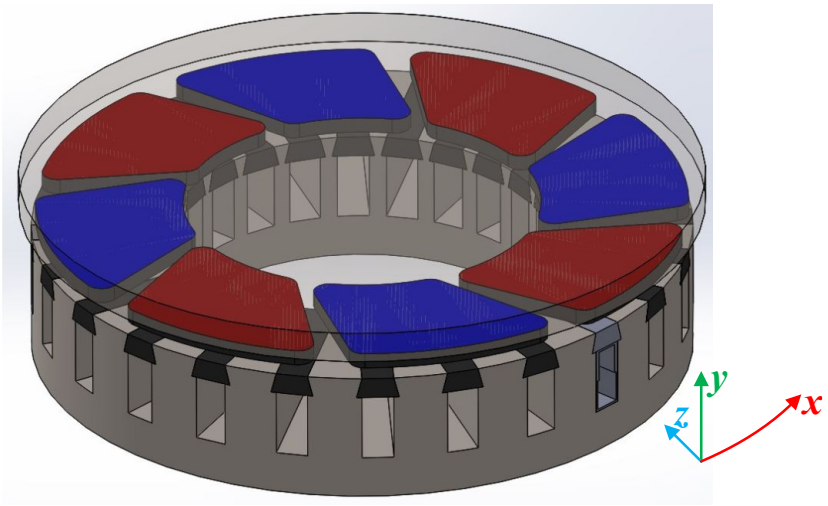

Figure 1: The analyzed three-phase 24-slot/8-pole integral slot AFPM machine.

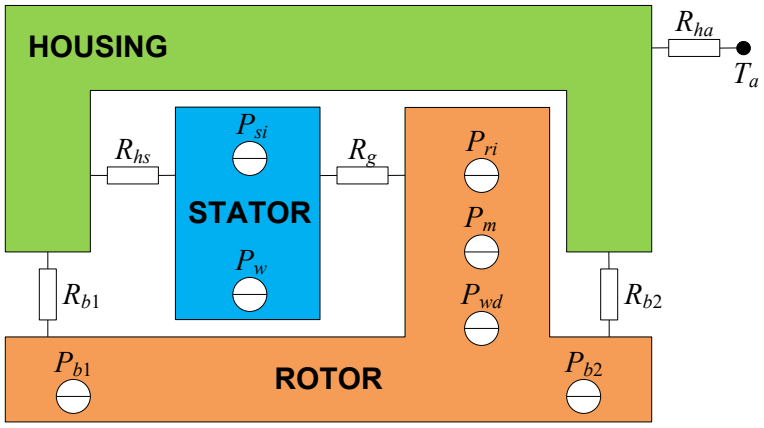

Figure 2: Analytical steady state thermal model of the half AFPM machine.

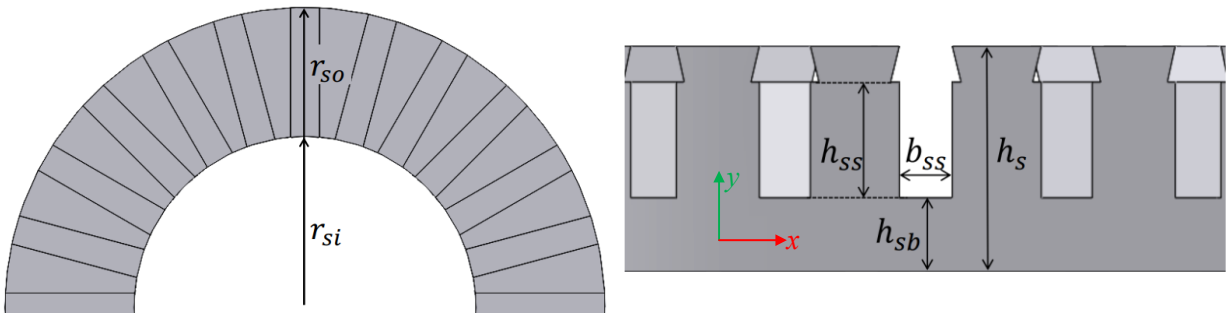

(a) (b)

Figure 3: (a) Top view and (b) Side view of the stator iron.

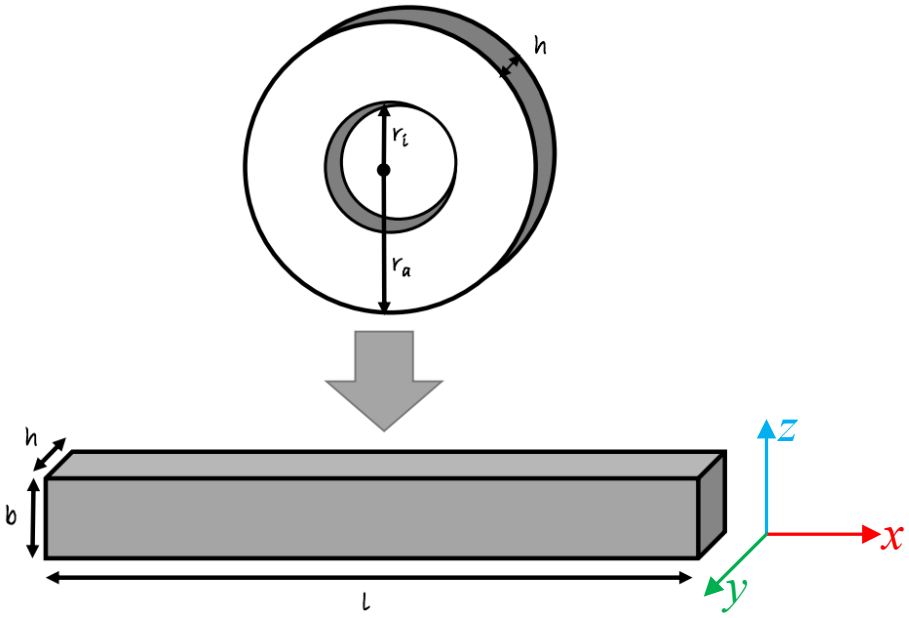

(a)

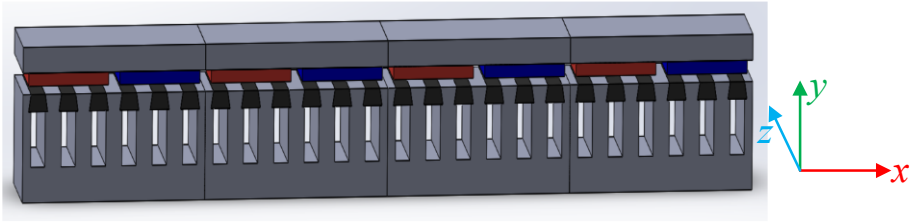

(b)

Figure 4: (a) 3-D to 2-D transformation and (b) 2-D linear model of the analyzed AFPM machine.

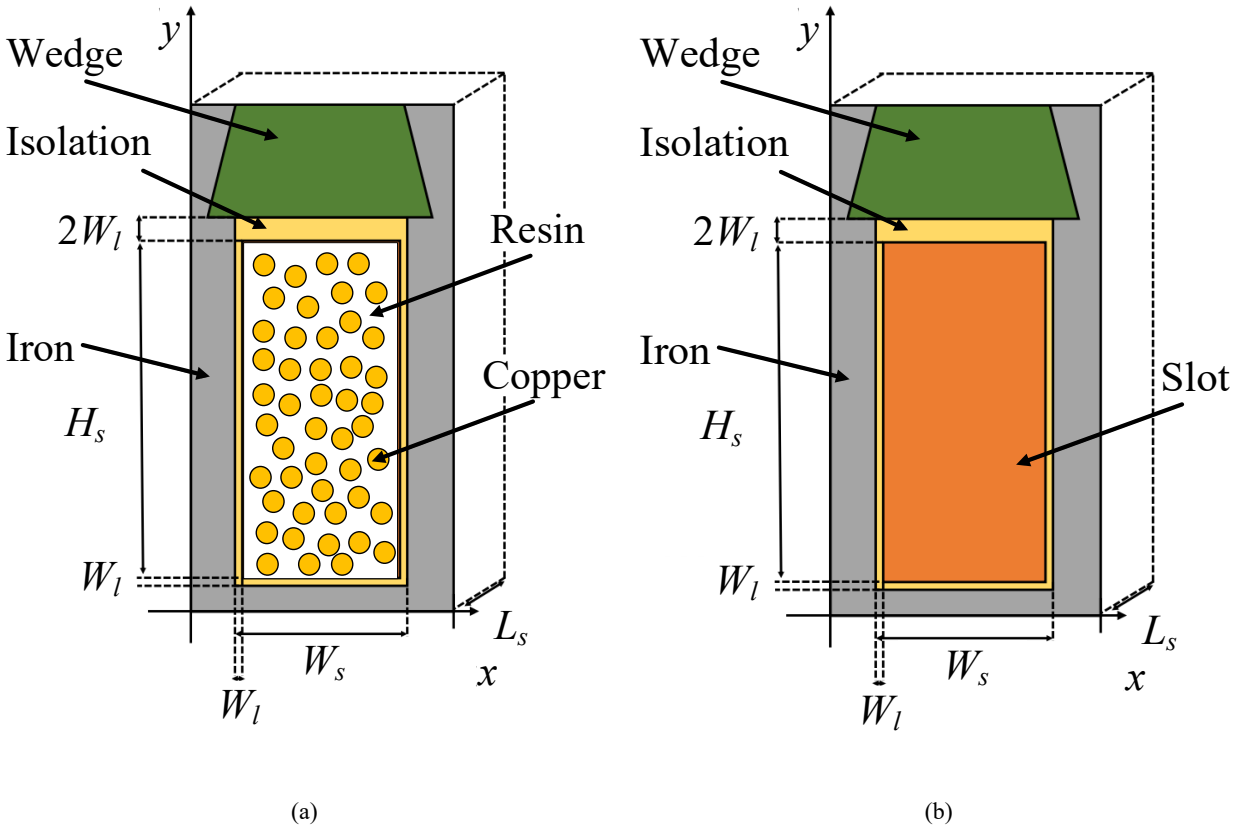

Figure 5: (a) Configuration of individual stator unit and (b) Illustration of the stator unit with layered winding model.

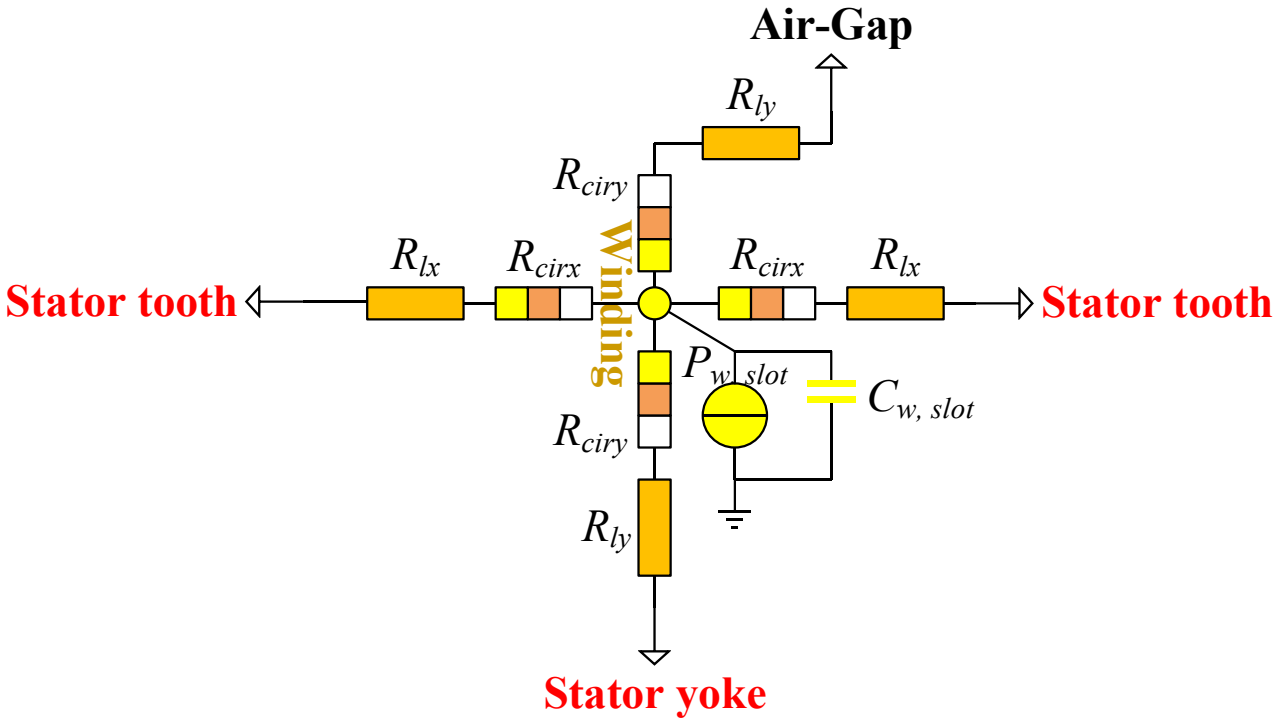

Figure 6: Single slot thermal model.

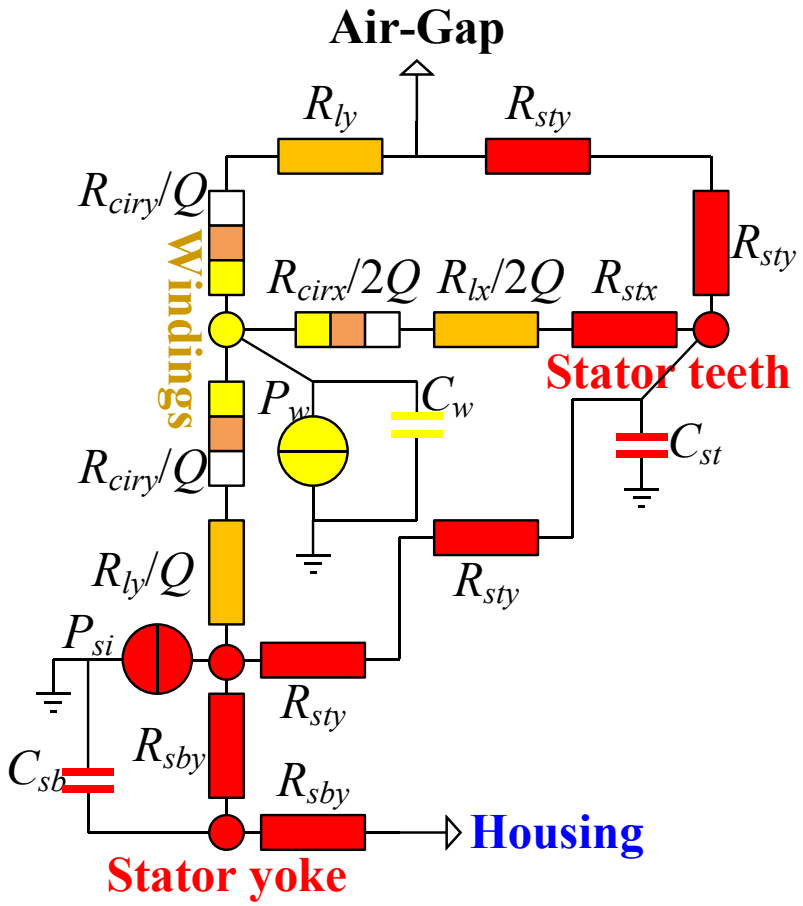

Figure 7: Stator thermal model.

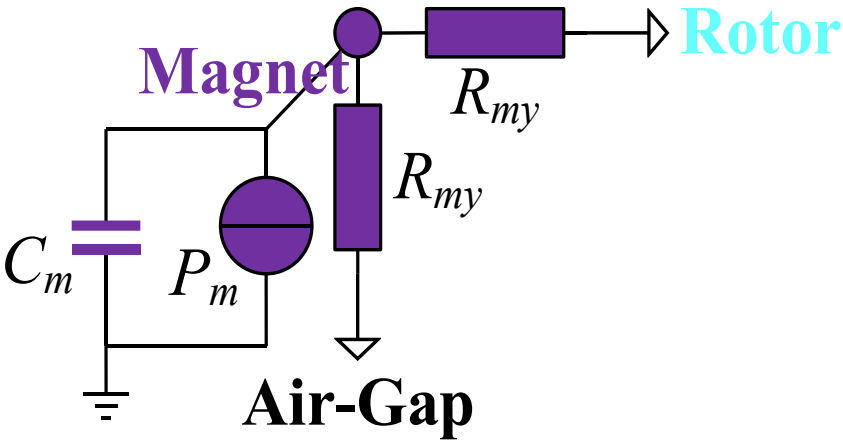

Figure 8: Permanent magnet thermal model.

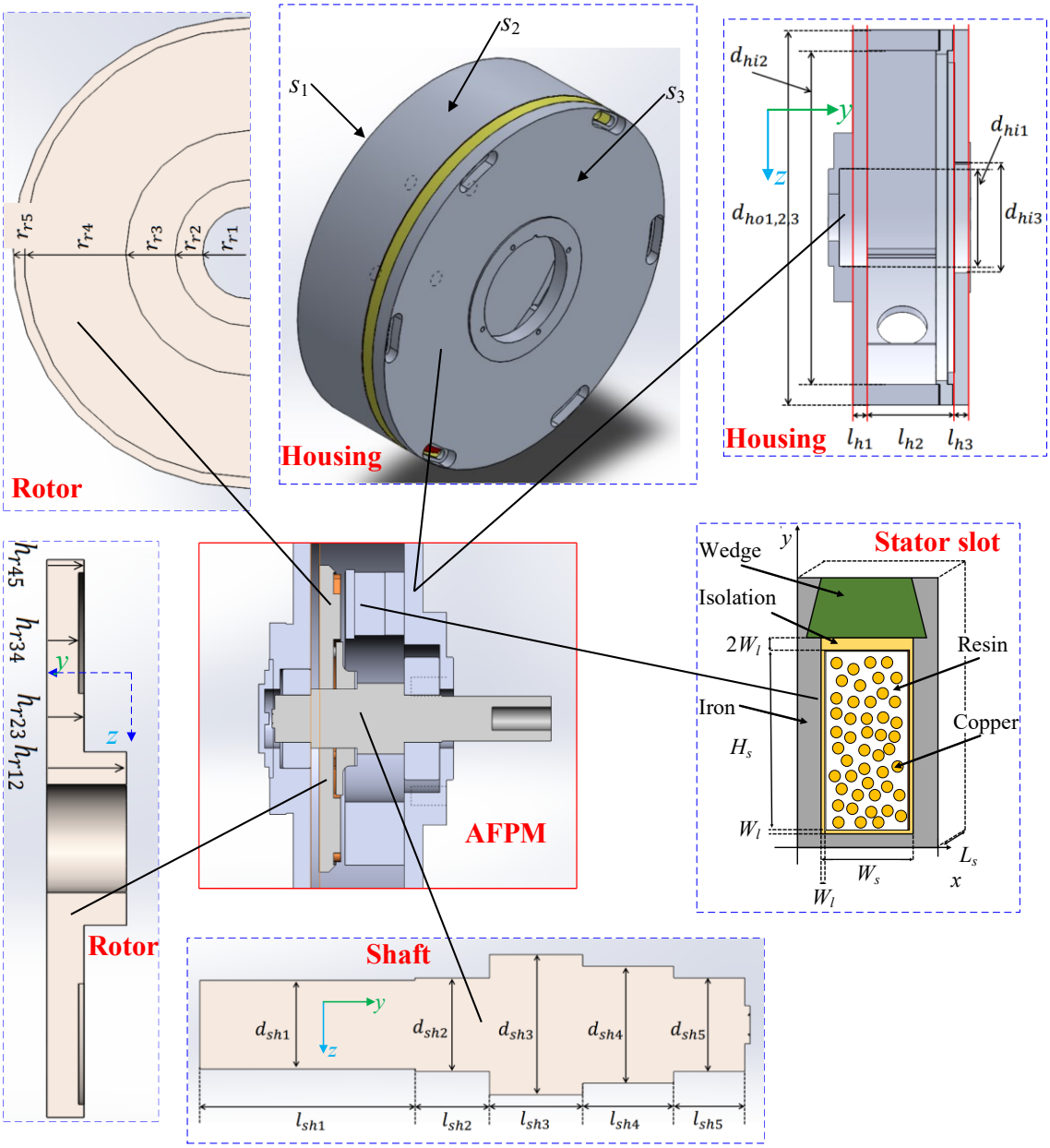

Figure 9: Cross-section and dimensions of the analyzed AFPM machine.

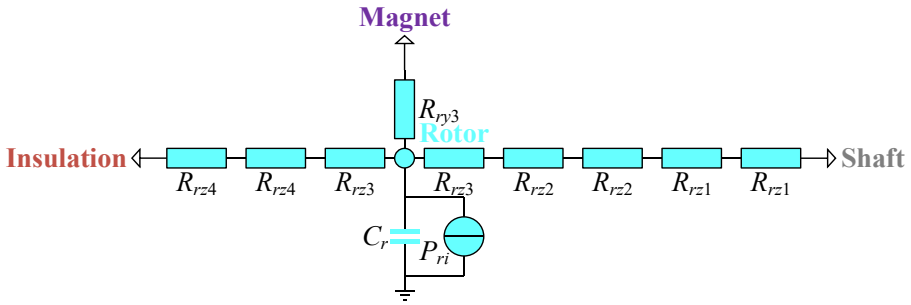

Figure 10: Rotor iron thermal model.

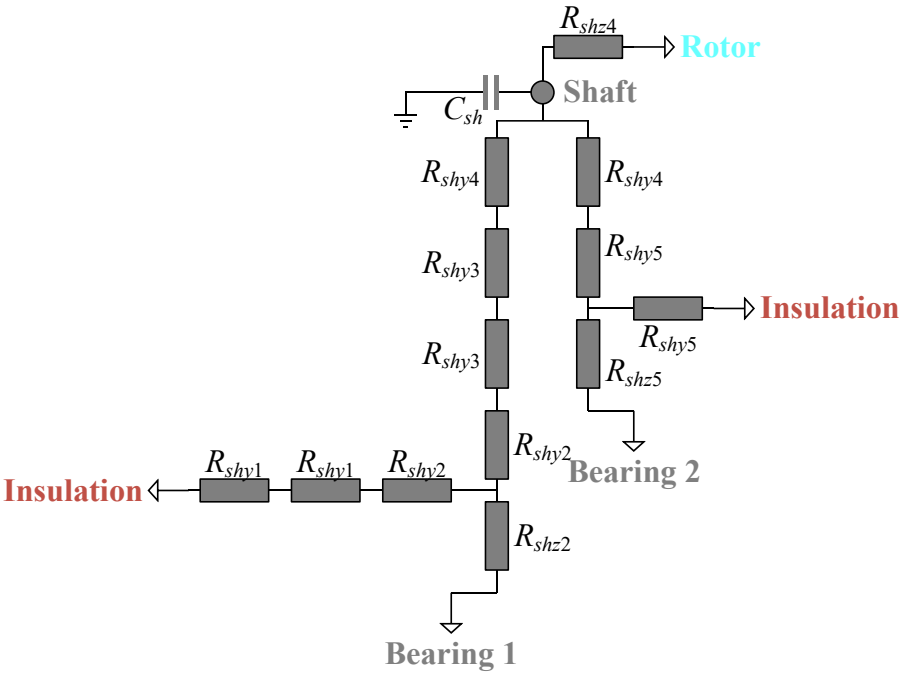

Figure 11: Shaft thermal model.

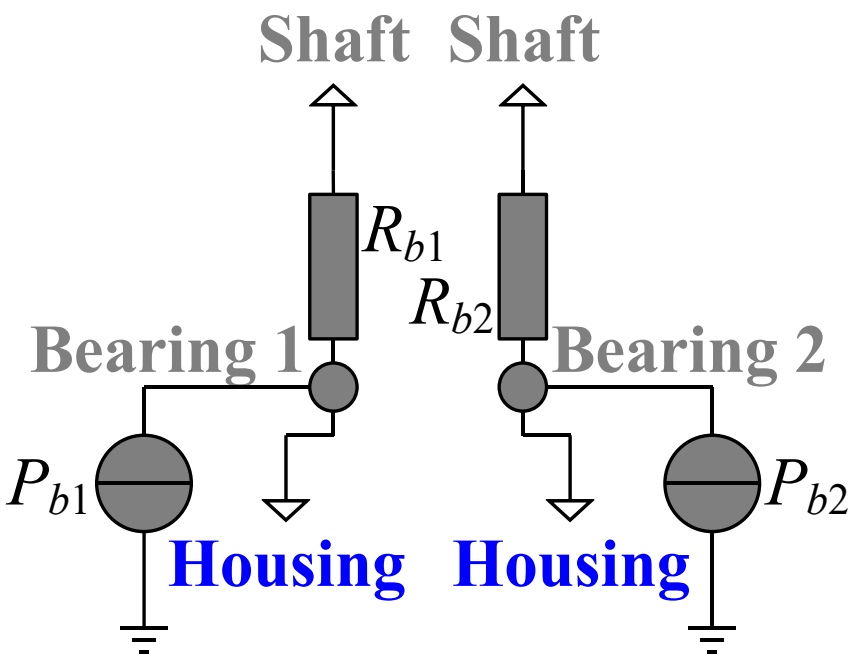

Figure 12: Thermal model of bearings.

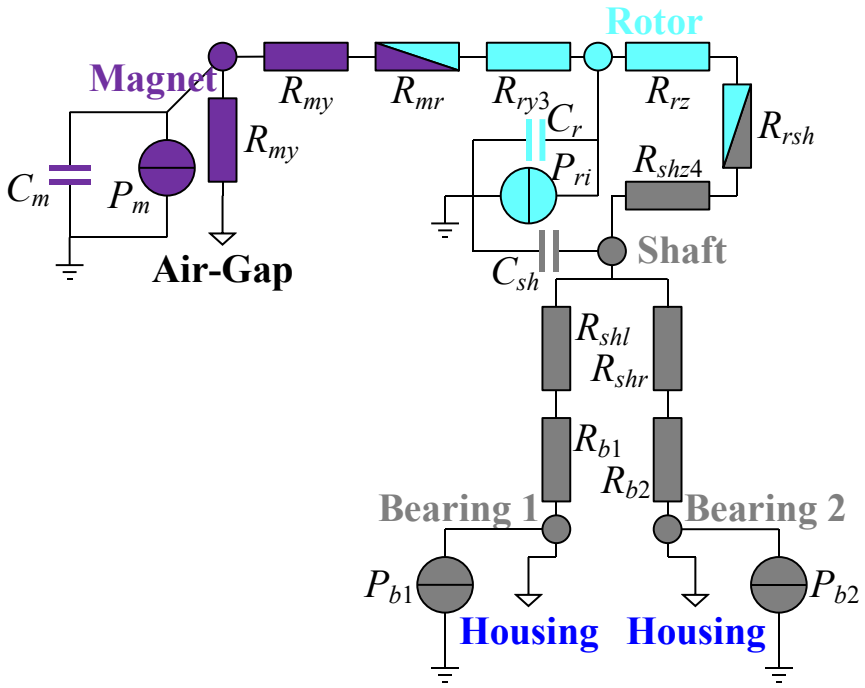

Figure 13: Thermal model of the rotor, shaft and bearings.

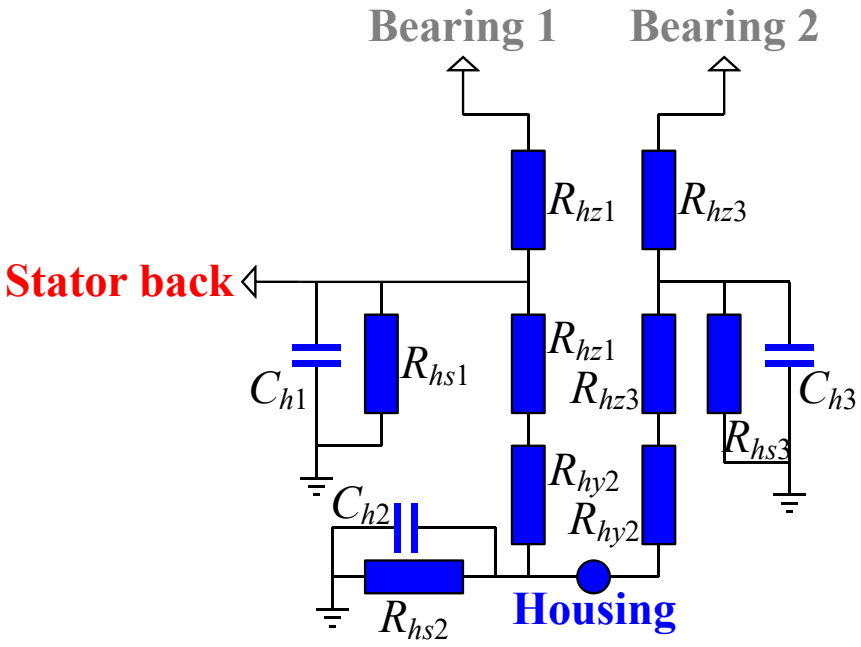

Figure 14: Thermal model of the housing.

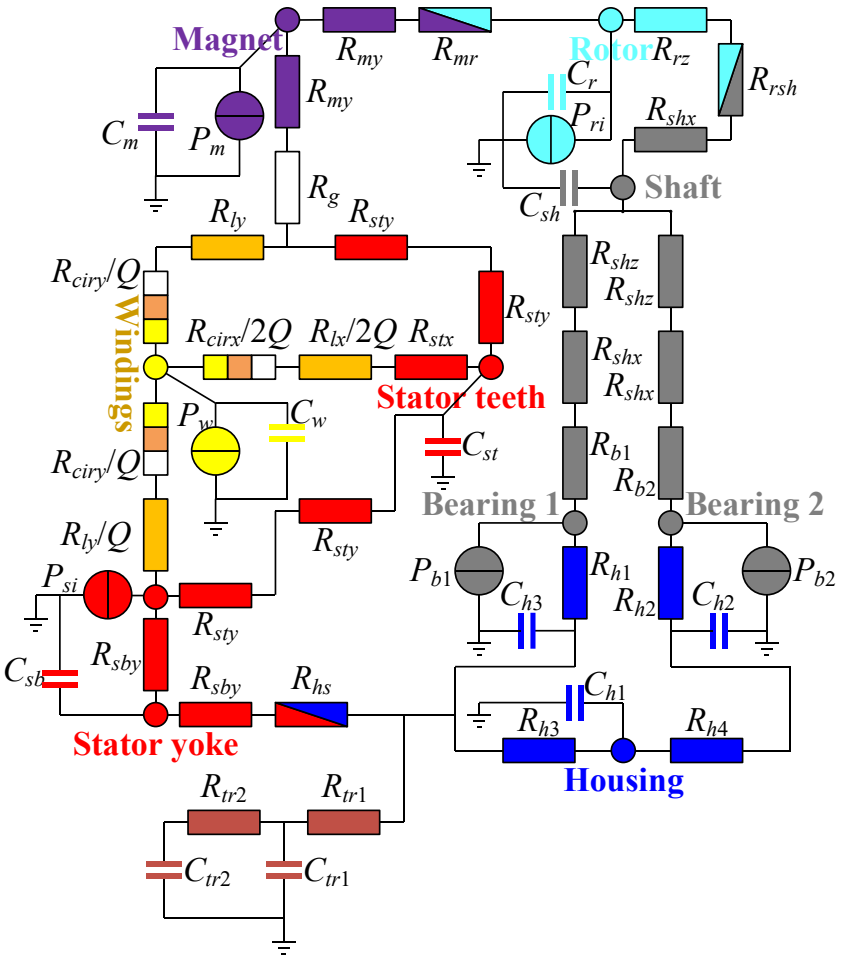

Figure 15: Illustration of the complete thermal model of the AFPM machine.

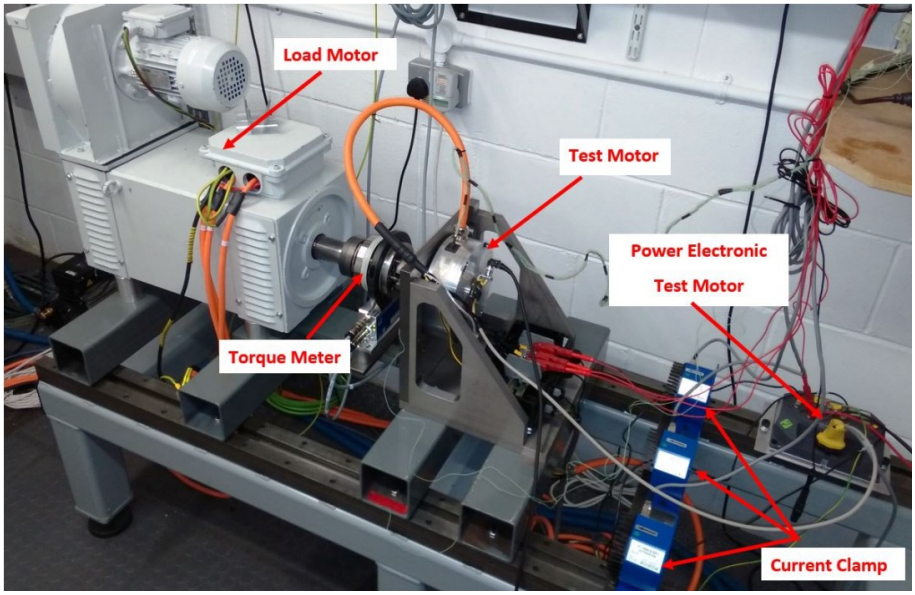

Figure 16: Photo of the test bench.

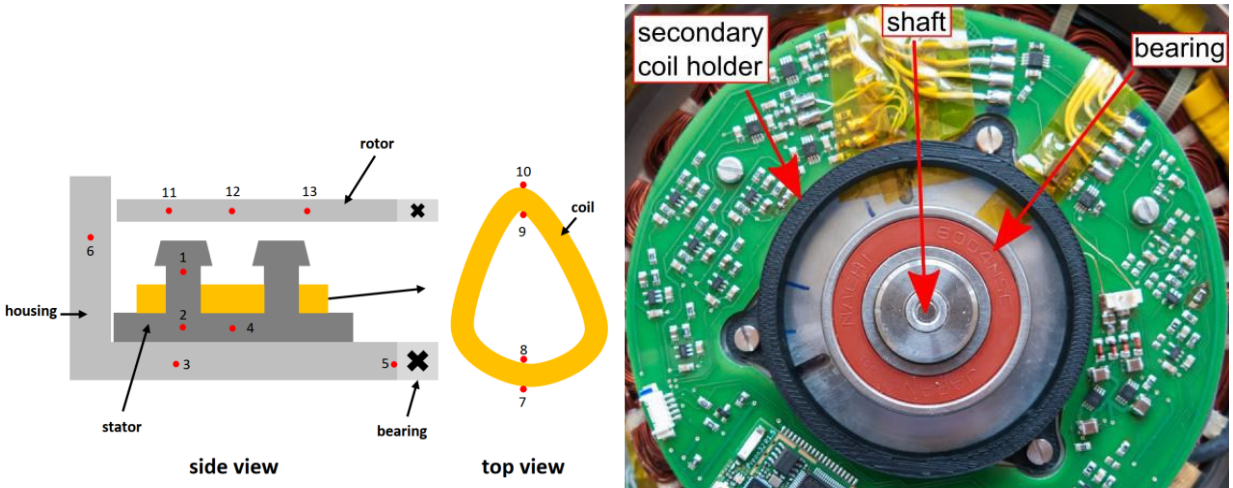

(a) (b)

Figure 17: (a) Illustration of thermocouple positions inside the test motor and (b) Photograph of the wireless sensor system used for on-rotor measurements.

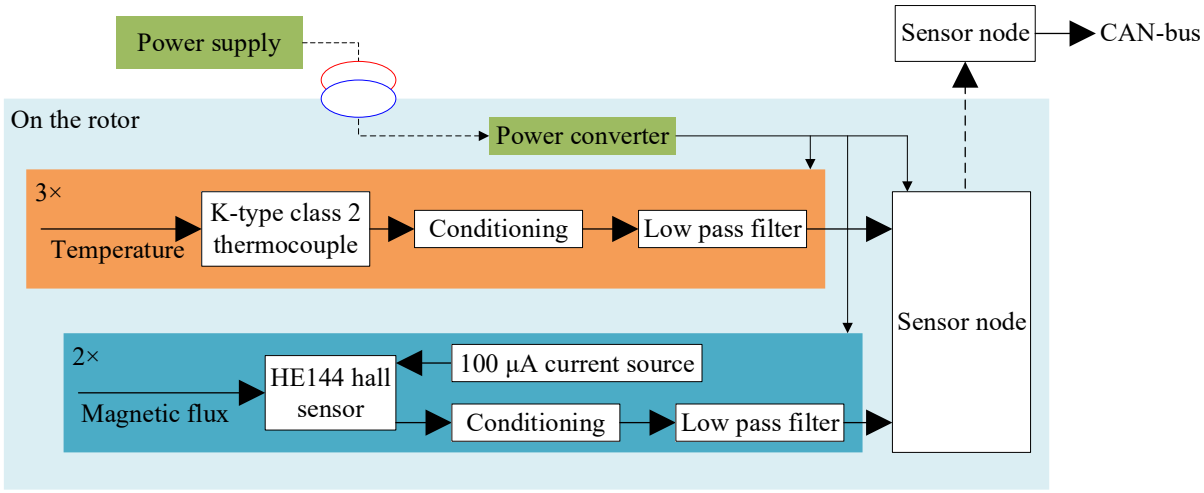

Figure 18: Structure of the wireless sensor measurement.

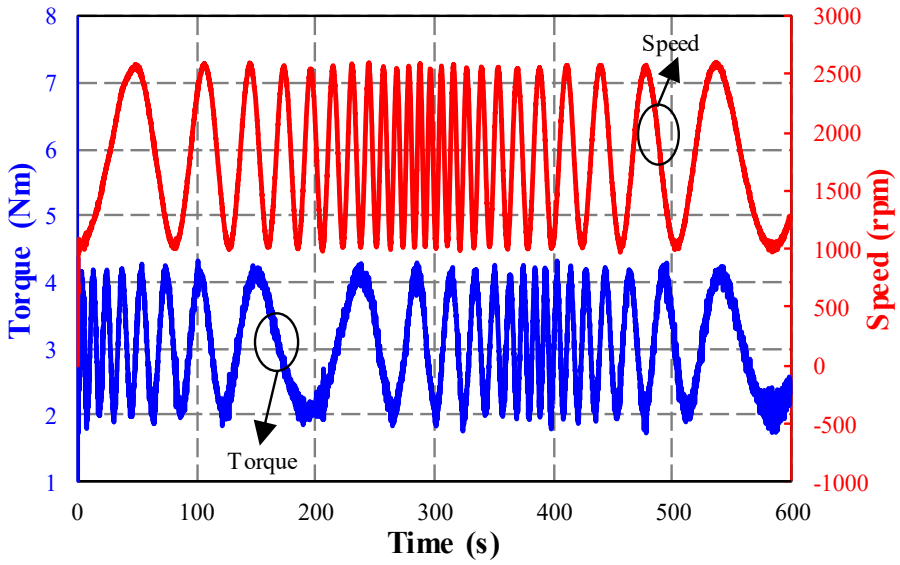

(a)

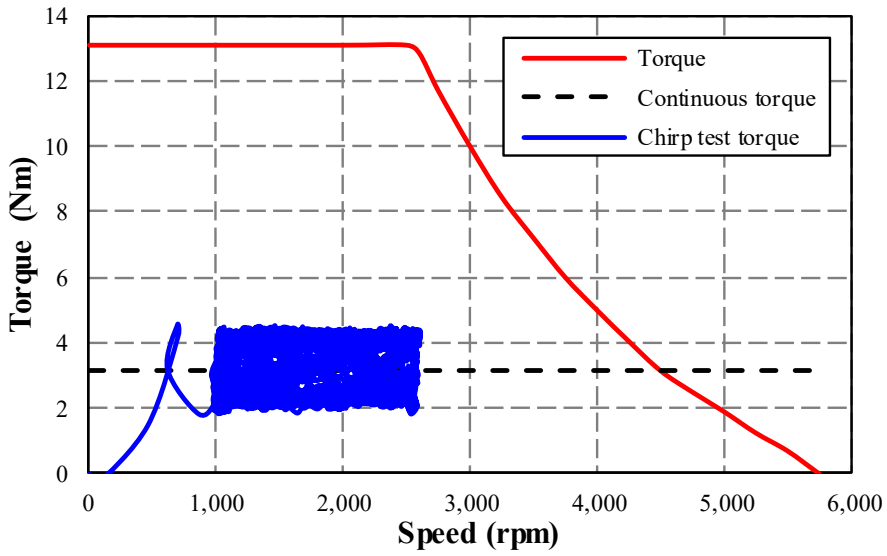

(b)

Figure 19: (a) Dynamic chirp test showing scaled motor speed and torque over the test cycle and (b) operating range of the chirp cycle on the motor speed torque map.

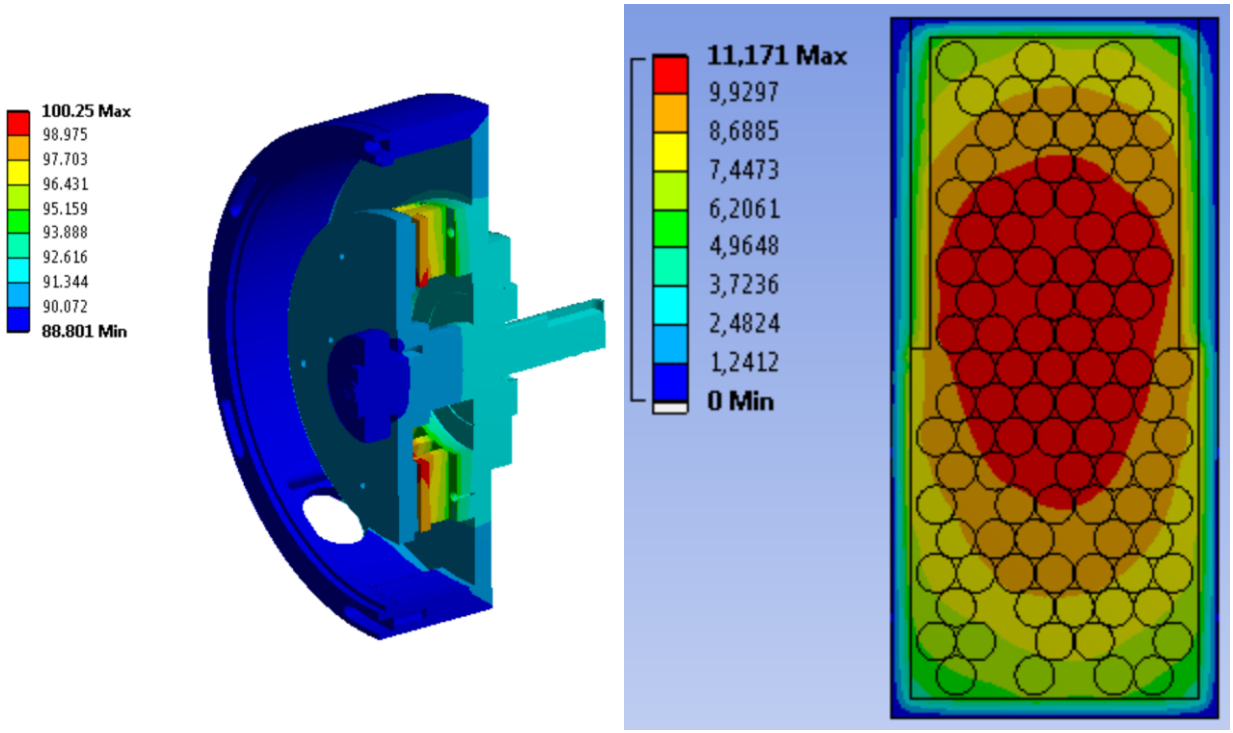

(a) (b)

Figure 20: (a) 3-D FE predicted temperatures for DC test and (b) 2-D FE predicted temperatures for DC test (k_r=1 W/mK, k_f=0.13 W/mK).

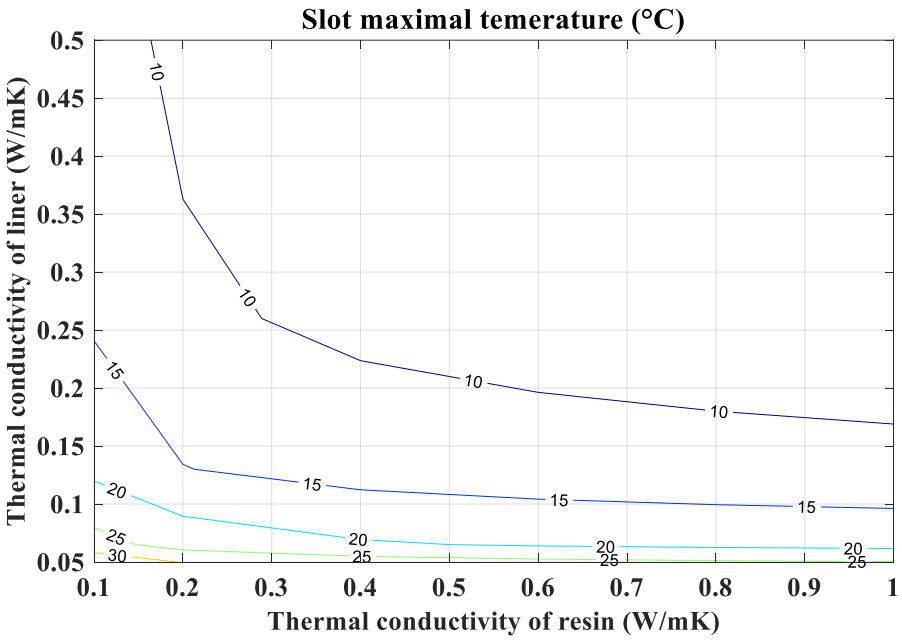

Figure 21: Variation of slot maximal temperature on the thermal conductivities of liner and resin (ambient temperature = 22 ℃).

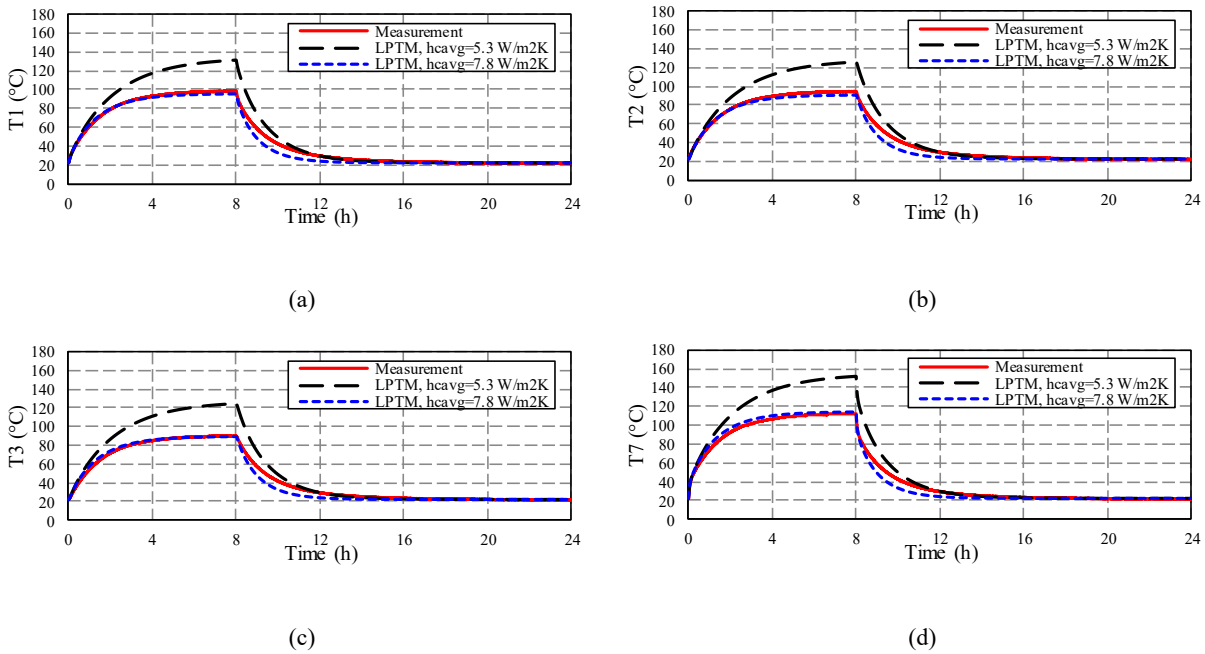

Figure 22: Comparison between the steady-state temperatures predicted by LPTM and measured values for (a) stator tooth T1, (b) stator back T2, (c) housing T3, (d) winding T7.

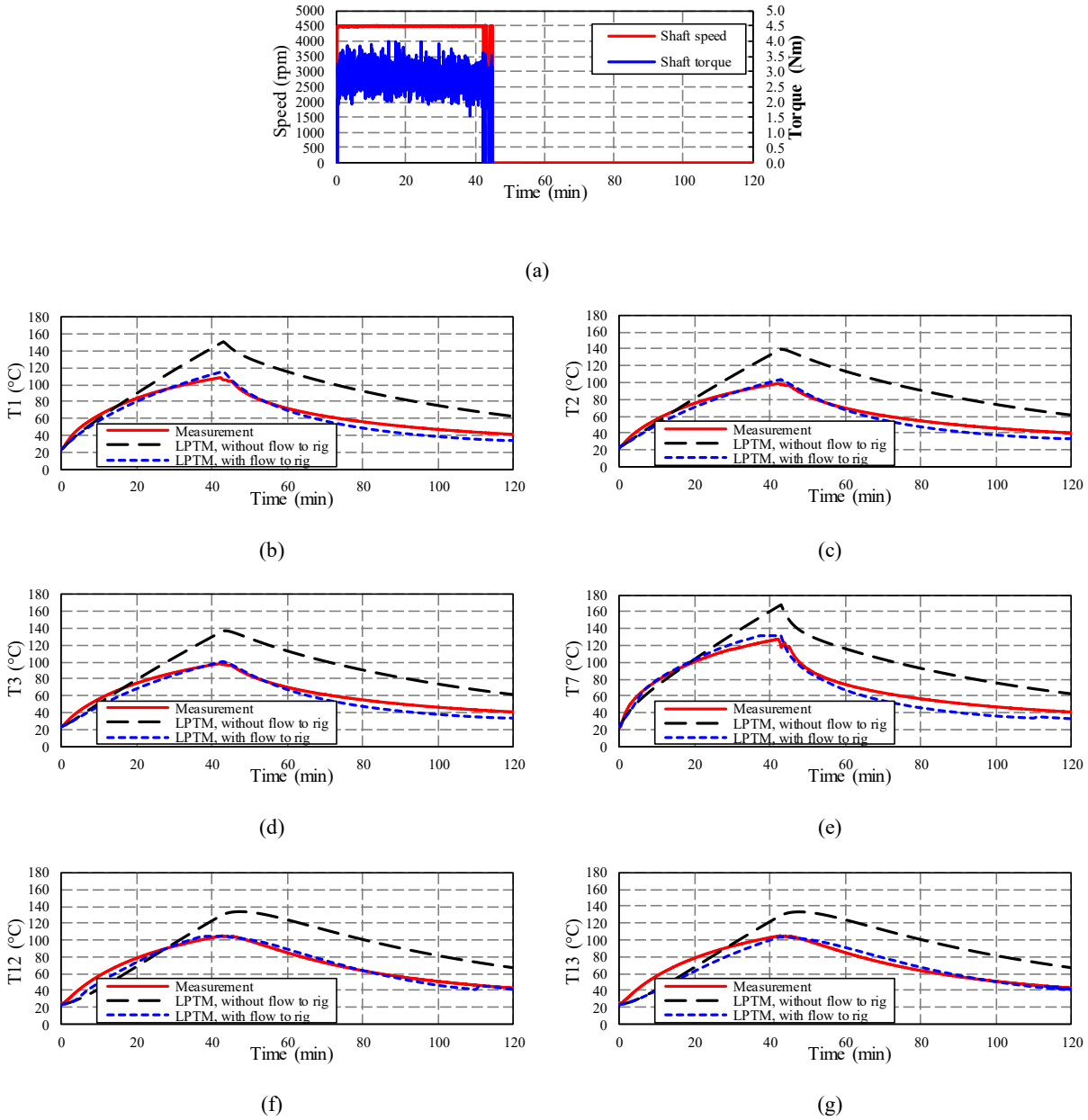

Figure 23: Comparison between the transient-state temperatures predicted by LPTM and measured values for (a) shaft speed / torque, (b) stator tooth T1, (c) stator back T2, (d) housing T3, (e) winding T7, (f) magnet T12 and (g) rotor iron T13.

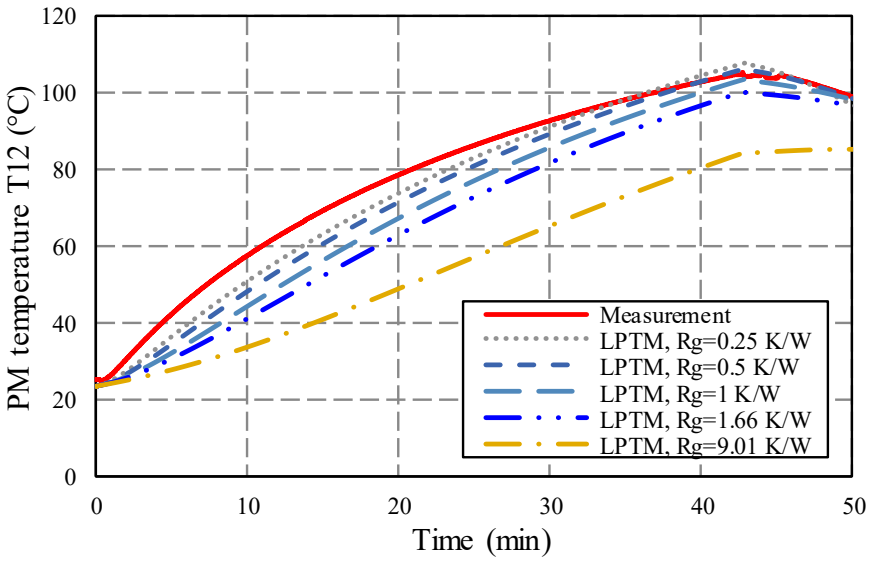

Figure 24: Variation of PM temperature for different air-gap thermal resistance.

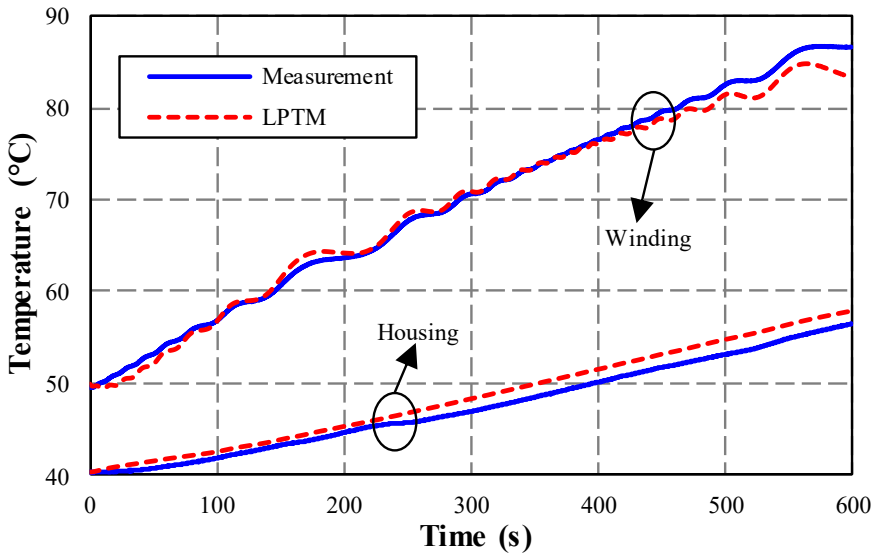

(a)

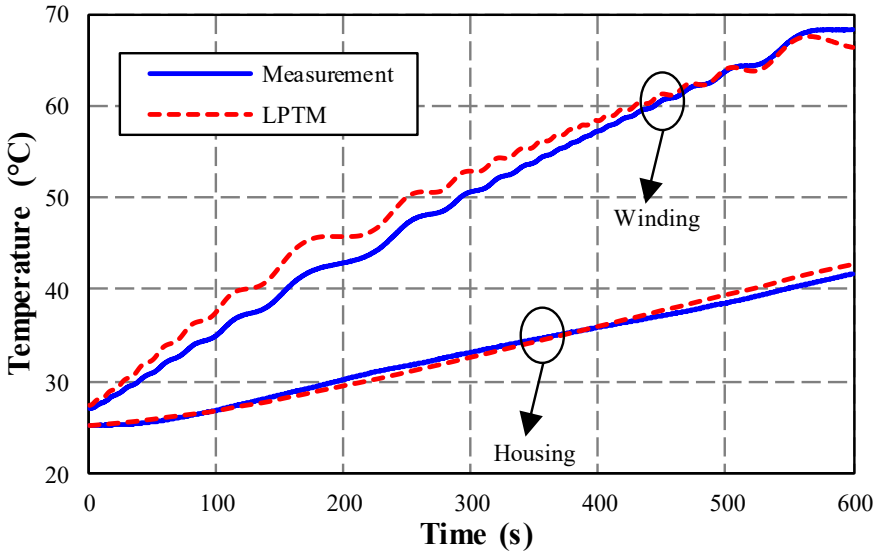

(b)

Figure 25: Measured and LPTM predicted winding and housing temperatures for (a) 50 °C start and (b) 25 °C start test.

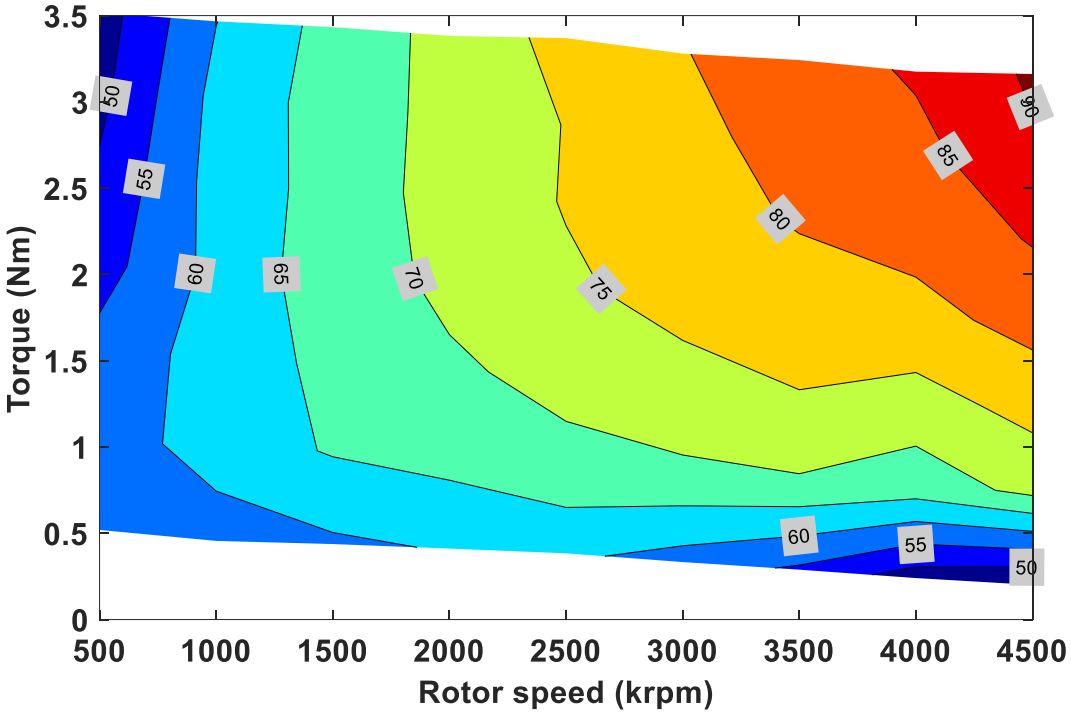

Figure 26: Measured efficiency map with rotor speed from 500 to 4500 rpm and loads from 0.5 to 3.5 Nm.